Modeling Interactions Between Flexible Flapping Wing Spars, Mechanisms, and Drive Motors

David B. Doman *
Chin Pei Tang †
Sean Regisford ‡

A system of dynamical equations is presented that allow micro air vehicle (MAV) ornithopter designers to match drive motors to loads produced by flexible flapping wing spars. The model can be used to examine the coupled system-level behavior of brushed DC motors, gear trains, and any number of linkages and flexible wing spars. A Lagrangian approach is used to derive the governing differential equations of motion for a class of ornithopter drive systems. Methods used to determine parametric constants contributing to generalized force components, which cannot be derived from first principles, are described. An example is presented where simulation results are compared to experimental measurements. The results show that the differential equations correctly predict major trends in observed motor speed and wing spar structural deformation over the course of each wingbeat. The results show that when pairing flight-weight motors and wings, significant variations in drive motor speed occur throughout each wingbeat. It is shown that coupling between motor speed, wing loads, and structural flexibility cause the aerodynamic forces encountered by the wing spars to depart from those predicted by rigid-spar and constant-velocity-motor-based kinematic simulations.

I. Introduction

A large class of micro-air vehicle (MAV) ornithopter flapping mechanisms consist of a brushed DC motor and gear train in combination with linkage elements, flexible wing spars, and wing surfaces. The aerodynamic and inertial loads produced by the wings, and the inertial loads produced by gear train and linkage elements, can significantly affect the instantaneous speed of the motor that drives them. Improperly matched motors and loads can result in repeated starting and stopping of the motor armature, which limits flapping frequency and reduces system performance. Thus, a systematic procedure for modeling the dynamics of this class of electro-mechanical aeroelastic systems is presented. One potential use for such a model is to serve as the basis for a vehicle design tool that matches drive motors to loads produced by flexible wings. A major objective of this exposition is to present a low-order dynamical model, of adequate fidelity, to predict the characteristics of the motion of flexible wing spars that are driven by ornithopter linkages and brushed DC motors.

There are three principal types of loads that a drive motor must overcome in an ornithopter application, viz., inertial, frictional, and aerodynamic. The inertial loads arise from both rigid body elements and flexible modes associated with the structural dynamics of the wings. The frictional loads arise from a combination of viscous and dry friction, where the former is due to light lubricating oils on the gear train and linkage elements. Additionally, the back-electromotive force, or back-EMF, inherent in all brushed DC motors produces a characteristic that from the point-of-view of the motor drive torque, behaves like viscous friction.

*Senior Aerospace Engineer, Control Design and Analysis Branch, 2210 Eighth Street, Ste. 21, Air Force Research Laboratory, WPAFB, OH 45433-7531, Email: David.Doman@wpafb.af.mil, Ph. (937) 255-8451, Fax (937) 656-4000, Associate Fellow AIAA

†Research Associate, University of Texas at Dallas, Erik Jonsson School of Engineering and Computer Science, 800 W. Campbell Rd., EC33, Richardson, TX 75080-3021, Summer Researcher, Control Design and Analysis Branch, Air Force Research Laboratory, WPAFB, OH 45433-7531, Email: chinpei@utdallas.edu

‡Aerospace Engineer, Control Design and Analysis Branch, 2210 Eighth Street, Ste 21, Air Force Research Laboratory, WPAFB, OH 45433-7531, Email: Sean.Regisford@wpafb.af.mil, Ph. (937) 255-8492, Fax (937) 656-4000, Senior Member, AIAA

Report Documentation Page

Form Approved
OMB No. 0704-0188

1. REPORT DATE	2. REPORT TYPE	3. DATES COVERED
SEP 2011		**00-00-2011 to 00-00-2011**

4. TITLE AND SUBTITLE	5a. CONTRACT NUMBER
Modeling Interactions Between Flexible Flapping Wing Spars, Mechanisms, and Drive Motors	5b. GRANT NUMBER
	5c. PROGRAM ELEMENT NUMBER
6. AUTHOR(S)	5d. PROJECT NUMBER
	5e. TASK NUMBER
	5f. WORK UNIT NUMBER
7. PERFORMING ORGANIZATION NAME(S) AND ADDRESS(ES) **Air Force Research Laboratory,Control Design and Analysis Branch,2210 Eighth Street, Ste. 21,Wright Patterson AFB,OH,45433-7531**	8. PERFORMING ORGANIZATION REPORT NUMBER
9. SPONSORING/MONITORING AGENCY NAME(S) AND ADDRESS(ES)	10. SPONSOR/MONITOR'S ACRONYM(S)
	11. SPONSOR/MONITOR'S REPORT NUMBER(S)

12. DISTRIBUTION/AVAILABILITY STATEMENT
Approved for public release; distribution unlimited

13. SUPPLEMENTARY NOTES
AIAA Journal of Guidance, Control and Dynamics, Vol. 34, No. 5, pp. 1457-1473, September-October 2011

14. ABSTRACT

15. SUBJECT TERMS

16. SECURITY CLASSIFICATION OF:			17. LIMITATION OF ABSTRACT	18. NUMBER OF PAGES	19a. NAME OF RESPONSIBLE PERSON
a. REPORT **unclassified**	b. ABSTRACT **unclassified**	c. THIS PAGE **unclassified**	**Same as Report (SAR)**	**28**	

The Lagrangian method is used to derive a system of governing differential equations that predict the coupled behavior of a brushed DC motor driving a gear train with an arbitrary number of stages, coupled to any number of linkages driving any number of flexible wing spars. Methods for obtaining the generalized forces associated with each degree-of-freedom are presented for the non-conservative forces and drive elements within the system.

Research in the area of flapping wing flight has been conducted by both the biological and engineering communities. These communities have leveraged one another's work and it is not uncommon for biologists to make use of aerodynamic theory and theoretical mechanics to characterize and understand the mechanisms that enable flight in insects or birds.[1–4] Likewise, the engineering community has taken advantage of the work of biologists to both devise machines that can approximate the motion of wings observed in nature and to control those motions in such a way as to enable a flapping winged aircraft to be stabilized and maneuvered as desired. Shyy et. al.[5] provides an overview of the work of both communities and provides a foundation for understanding the physics of flapping flight at low Reynolds numbers.

The current state of technology allows one to design and construct ornithopters using ad-hoc methods to match loads to motors. A large amount of the work reported in the literature describes the construction of flying prototypes. For instance, the flapping wing aircraft known as DelFly[6] was developed at TU Delft in the Netherlands and is capable of controlled forward flight and hover. A similar commercially available aircraft, known as the WowWee Dragonfly[a], is an ornithopter that makes use of four flapping wing surfaces to provide propulsion for the aircraft. Researchers at the Naval Postgraduate School developed an aircraft that replaces conventional propulsion mechanisms[7] with flapping wings. Recently, Gerdes *et. al*[8] exhaustively enumerated the flapping wing aerial vehicles that have had at least one successful reported flight. In a preliminary study[9] on tailless hover-capable ornithopter design, it was found that such aircraft present major challenges associated with trim and control. The work presented here shows the importance of characterizing interactions between loads and drive motors, and the effects that these interactions have upon the aerodynamic forces. It is important for control law designers to be aware of the presence of these interactions and their impact upon the cycle-averaged behavior of the aerodynamic forces and moments.

In terms of designing drive mechanisms for flapping wings, it is desirable to minimize the number of on-board actuators in order to minimize gross take-off weight. Closed-loop mechanisms such as four-bar linkages have the desirable quality of creating flapping or rocking motion using a single drive actuator. Extensive work has been reported in this area. Researchers have used synthesis-based or optimization-based methods to design mechanisms that *match* the wing motion produced by many flying biological species in a kinematic sense. For instance, the series of designs by Agrawal, et.al.[10,11] attempted to optimize various mechanism designs, based upon kinematic or quasi-static models of the mechanism motion, in order to match the motion generated by some of the representative flying species. Similarly, Rahmat *et. al*[12] synthesized and fabricated a spherical four-bar mechanism to mimic the figure-8 wing stroke motion observed in a number of natural flyers. While they showed simulation and experimental results,[13] their proof-of-concept prototype only qualitatively showed the feasibility of such design. Raney and Slominski[14] developed a ground-test apparatus that could vary the wing kinematics produced by a machine that approximated the wing motion observed in hummingbirds. The experiment focused on the control of the wingtip trajectories by varying the amplitude and phase of waveforms applied to two electrodynamic actuators. Chung et.al.[15] investigated the use of central pattern generators to control the three dimensional motion of the wings of a 10 degree-of-freedom robotic bat in a wind tunnel experiment. Other researchers[16–18] have investigated the problem of optimizing wingbeat kinematics for power or aerodynamic efficiency.

In the above efforts, however, the interactions between the drive elements and wing flexibility were not mathematically modeled when optimizing mechanisms for matching the observed motion of natural flyers. In the present exposition, it is shown that the idealized kinematic behavior of a linkage and rigid wing spar driven by a constant velocity DC motor is quite different from that produced by a system where a torque-limited flight-weight motor drives flexible wing spars. As will be shown in the present work, the ability to prescribe wingbeat kinematics in flight-weight systems will not normally be possible because of torque limits and dynamic interactions between drive and wing components. One of the conclusions of the present study is that the entire system, from drive motor to wing, must be integrated into the model when attempting to match the observed motion of biological systems with a flight-weight mechanical system.

In terms of overall flight control, Deng et.al.[19,20] designed, modeled, simulated, and produced a cycle-averaged control design for a conceptual biomimetic flapping wing robotic aircraft. Khan and Agrawal[21]

[a] http://www.wowwee.com/en/products/toys/flight/flytech/dragonfly

used a time-averaged control approach in conjunction with a differential flatness based control scheme to design a longitudinal flight controller for a flapping-wing MAV. DeLeo and Deng[22] presented a four-wing aircraft design based on a dragonfly that featured a single rotary motor that drove the wings in the stroke-plane, a tunable phase difference between the forewings and hindwings using a variable length coupler link, and passive wing rotation about the spar. In the above control related studies, the dynamic interactions between the drive components and the flexible and aerodynamic loads were not considered. Because such interactions affect the aerodynamic forces and moments produced by the wings, they will also affect one's ability to control the aircraft.

Finally it is worth noting that there is line of research pursued by Wood[23] et.al. that has focused on the development of piezoelectrically powered micro mechanical insects. The first takeoff of an insect-scale flapping wing MAV was achieved by an aircraft called RoboFly that was developed at Harvard University by Wood et.al.[24] Avadhanula, et.al.[25] modeled a flapping wing piezo-electrically actuated electromechanical subsystem system using a Lagrangian approach. While, piezoelectrically actuated flapping wing aircraft are an important class of vehicles with a promising future, the work presented here is focused on the fundamentally different dynamic interactions that occur between DC motor powered gear-trains, linkage-based mechanisms, and flexible wing spars.

The remainder of the paper is structured as follows: Section II presents a description of the components that comprise the class of systems under consideration. The Lagrangian formalism enables the analysis of the interactions between each subsystem, in terms of energy, and is presented in Section III. Section IV evaluates the equation-of-motion of the system using Lagrange's equation. Taking advantage of the additive properties of derivatives, the equations-of-motion are derived in a modular fashion. In Section V, nonconservative generalized forces, such as drive-motor torque, modal damping, frictional, and aerodynamic forces are derived using the principle of virtual work. The information required to evaluate these terms are supported, in some cases, by experimental measurements. Finally, in Section VI, simulation results are critically compared to experimental results generated by the system described in Section II.

II. Description of a Bench-Test Article

The framework developed in this manuscript is directly applicable to a large class of MAV ornithopter designs; however, the simulation and experimental results that are presented, apply to a specific test article that consists of components of a prototype aircraft considered by Doman et.al.[9] In order to introduce the reader to the class of systems under consideration, a specific bench test article will now be described. The bench-test article and some of the supporting measurement apparatus is shown in Fig. 1. For the purpose of the analysis in this paper, the system is considered to be rigidly mounted to the bench. The system consists of a coreless brushed DC motor driving a set of compound gears, which in-turn drives a four-bar mechanism that imparts rocking motion to a flexible wing spar.

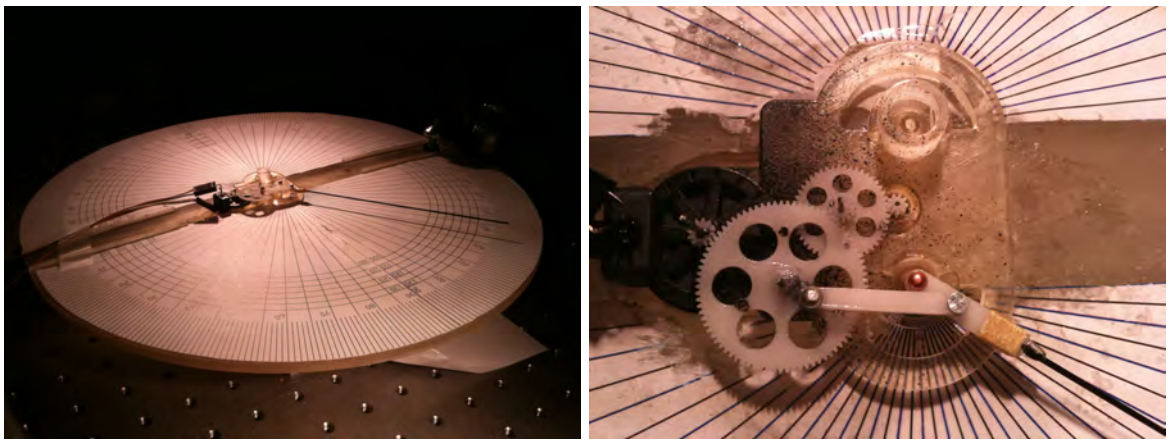

(a) Bench-test article

(b) Enlarged view of driving mechanism (diameter of large gear is 2.49 cm)

Figure 1. Experimental Setup

The fuselage frame was produced from a CAD model using a 3-D printer. The gears came from a commercial source. The linkage elements were custom machined from Delrin. The linkage pins were made from commercially available 1/16 inch (.158 cm) aluminum rivets. The spar was made from commercially available 0.037 inch (.09398) carbon fiber rod cut to 13cm in length. The spar was attached to the rocker arm of the linkage using a Kevlar wrap that was saturated with cyanoacrylate adhesive. The fuselage frame also incorporated a custom-made 16 slot optical encoder. The encoder meshed with the linkage crank gear to measure the overall system's angular velocity. Because of the choice of gear ratios, the encoder rotated at the same velocity as the stage 1 gear. The motor power was supplied by a regulated voltage source. A high speed camera system was used to capture the motion of the system at 2000 frames per second and the images were used to critically compare the motion of the simulation model with that observed in the experiments.

The development that follows applies to a general class of ornithopter flapping mechanisms. The bench-test mechanism described above was used to experimentally validate the equations of motion for a special case.

III. Modeling and Lagrangian Formulation of Each Subsystem

The overall system consists of the following components: a motor, gear-train, four-bar linkage, and a flexible wing spar. For the purpose of this paper, the fuselage is assumed to be rigidly mounted to a bench, thus a fuselage-fixed coordinate frame is taken to be an inertial frame. The motor and the linkage line-of-centers are also taken to be fixed with respect to the fuselage frame.

In what follows, the kinetic energy (T) and/or potential energy (V) of each subsystem is considered. The Lagrangian of a mechanical system is defined as:

$$\mathcal{L} \triangleq T - V \tag{1}$$

In a subsequent section, the energy of all of the subsystems are summed together, and the equations-of-motion of the overall system are determined using Lagrange's equation.

A. DC Motor

First, a model of a brushed DC motor is considered. According to Ogata,[26] the torque produced by a motor is proportional to the current flowing through the windings:

$$\tau_\theta = K_T i_a \tag{2}$$

where K_T is the motor torque constant, and i_a is the current. The back-EMF produced by the motor as a result of its angular velocity can be described as:

$$e_b = K_b \dot{\theta} \tag{3}$$

where K_b is the back-EMF constant, θ is the angular position of the motor armature, and $\dot{\theta}$ is its angular velocity. The differential equation governing the dynamics of the armature circuit is given by:

$$L_a \frac{di_a}{dt} + R_a i_a + e_b = e_a \tag{4}$$

where L_a is the inductance of the motor, R_a is the resistance of the armature, and e_a is the voltage applied to the armature. According to Ogata,[26] motor inductance is typically very small; thus, $L_a \approx 0$. Using the small inductance approximation and solving for i_a from Eq. (4) yields:

$$i_a = \frac{e_a - e_b}{R_a} \tag{5}$$

Substituting Eqs. (5) and (3) into Eq. (2) allows one to solve for the net torque produced by the motor,

$$\tau_\theta = \frac{K_T}{R_a} e_a - \frac{K_T K_b}{R_a} \dot{\theta} \tag{6}$$

Note that the torque is dependent on the input voltage e_a. The back-EMF and drive torques form a portion of the total generalized force associated with the rigid body degree-of-freedom θ.

The rotation of the motor armature contributes kinetic energy to the mechanical system according to:

$$T_m = \frac{1}{2} J_a \dot{\theta}^2 \tag{7}$$

where J_a is the mass moment of inertia of the armature and spindle about the axis-of-rotation. Since the motor does not contribute to the potential energy of the system, the Lagrangian of the *DC motor subsystem* is given by:

$$\mathcal{L}_m = T_m = \frac{1}{2} J_a \dot{\theta}^2 \tag{8}$$

B. Gear Train

Many ornithopter designs use compound gear trains to reduce the speed of the motor to achieve a target wing flapping frequency. The overall speed reduction and torque amplification can be tuned, within limits, to match the torque of the motor to the loads produced by the wing and the mechanism.

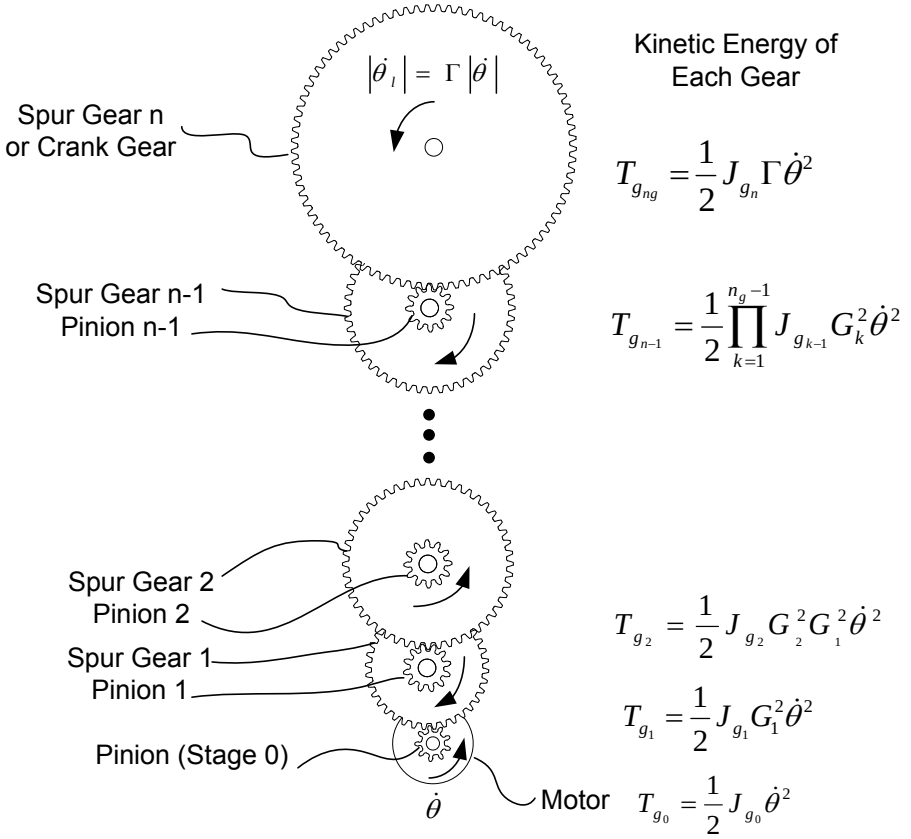

Figure 2. Compound Gear Train Transmission

Figure 2 shows a compound gear train that consists of n_g stages. The stage 0 gear in the train is a pinion fixed to the motor armature. The armature pinion, which has p_0 teeth, meshes with periphery of a first stage compound gear that has t_1 teeth. At each stage, the pinion of each compound gear meshes with the spur gear of the subsequent stage to incrementally increase mechanical advantage and reduce speed until the final crank gear stage n_g is reached. The crank gear stage n_g then forms the crank for the four-bar linkage portion of the drive-train. The total speed reduction from the pinion to the crank is given by:

$$\dot{\theta}_l = \left(\prod_{k=0}^{n_g} G_k \right) \dot{\theta} \tag{9}$$

where $\dot{\theta}_l$ is the crank angular velocity of the four-bar linkage, n_g is the number of gears in the gear train, G_k is the gear ratio of the k^{th} stage, which for a given gear pitch, is given by:

$$G_k = \begin{cases} 1, & k = 0 \\ \frac{p_{k-1}}{t_k}, & k = 1, 2, \cdots \end{cases} \tag{10}$$

where p_{k-1} is the number of teeth on the pinion of compound gear $k-1$, and t_k is the number of teeth on the spur gear k. For convenience, the overall gear ratio from the motor to the crank gear is defined as:

$$\Gamma \triangleq \prod_{k=0}^{n_g} G_k \tag{11}$$

Excluding the crank gear, the total kinetic energy and the Lagrangian of the $n_g - 1$ gears and the pinion attached to the motor spindle, is given by:

$$\mathcal{L}_g = T_g = \frac{1}{2} \left[\sum_{k=0}^{n_g-1} \prod_{j=0}^{k} J_{gk} G_j^2 \right] \dot{\theta}^2 \tag{12}$$

where J_{g0} is the mass moment of inertia of the pinion, and J_{gk} is the mass moment of inertia of each compound gear in the gear train. Note that the crank gear energy is not included in T_g because it is included in the energy of the linkage that is derived in the subsequent section. Since there is no potential energy contribution from the gear-train, the Lagrangian of the *gear train subsystem* is simply $\mathcal{L}_g = T_g$:

For the system introduced in Section II, $n_g = 2$. Hence:

$$\mathcal{L}_g = T_g = \frac{1}{2}(J_{g0} + J_{g1} G_1^2)\dot{\theta}^2 \tag{13}$$

It is worthwhile to note that the kinetic energy of other rotating components, such as encoder wheels used to measure position or speed, can be included by lumping the mass moment of inertia of these components with the mass moment of inertia of any gears that rotate at the same speed. For example, the encoder wheel used in the experiments performed under this work, moves at the same speed as the first stage compound gear. Thus, the effective mass moment of inertia can be computed from the following sum:

$$J'_{g1} \triangleq J_{g1} + J_e + J_{ep} \tag{14}$$

where J_e and J_{ep} represent the mass moments of inertia of the encoder wheel and the pinion attached to the encoder wheel respectively.

C. Four-Bar Linkage

Figure 3 defines the elements of a four-bar linkage for the class of systems under consideration. The physical structure of the crank gear, viz., gear stage n_g, forms the crank of the four-bar linkage. A pin of mass m_p connects the crank gear to a coupler bar of mass m_2 and mass moment of inertia about its own center-of-mass of I_2. The coupler bar is connected to a rocker arm of mass m_3 and mass moment of inertia I_3 by a pin of mass m_p. The line that connects the center-of-rotation of the crank gear and the pivot point of the rocker-arm is called the line-of-centers, whose length is denoted as l_0.

Due to the closed-loop kinematic constraints formed within the linkage, the time evolution of the generalized coordinates of the crank gear angle θ_l, coupler angle α_l, and rocker angle ϕ_l are highly coupled. However, it is well-known that a four-bar linkage is a single-degree-of-freedom system, permitting one to express α_l and ϕ_l in terms of θ_l. Hence, the objective of this section is to establish the total kinetic energy of all the linkage elements in terms of the motor angular velocity $\dot{\theta}$.

1. *Four-Bar Linkage Kinematics*

To solve the kinematic problem of the four-bar linkage under consideration, the loop-closure constraint equation is written as:

$$l_1 \cos\theta_l + l_2 \cos\alpha_l = l_o + l_3 \cos\phi_l \tag{15}$$

$$l_1 \sin\theta_l + l_2 \sin\alpha_l = l_3 \sin\phi_l \tag{16}$$

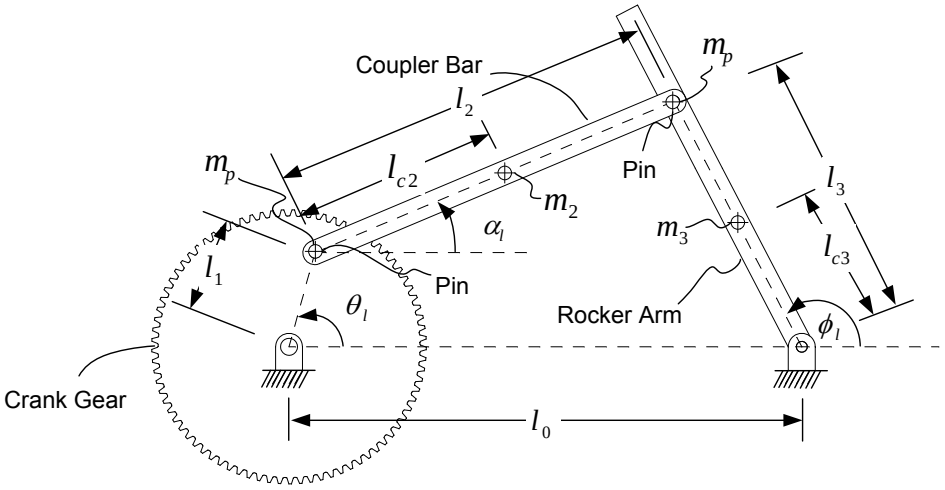

Figure 3. Four Bar Linkage

Solving for the terms containing α_l yields:

$$l_2 \cos\alpha_l = l_o + l_3 \cos\phi_l - l_1 \cos\theta_l \tag{17}$$

$$l_2 \sin\alpha_l = l_3 \sin\phi_l - l_1 \sin\theta_l \tag{18}$$

Eliminating α_l by squaring and summing Eqs. (17) and (18) yields the Freudenstein Equation:

$$K_1(\theta_l)\sin\phi_l + K_2(\theta_l)\cos\phi_l + K_3(\theta_l) = 0 \tag{19}$$

where,

$$K_1(\theta_l) = -2l_1 l_3 \sin\theta_l \tag{20}$$

$$K_2(\theta_l) = 2l_3(l_o - l_1\cos\theta_l) \tag{21}$$

$$K_3(\theta_l) = l_o^2 + l_1^2 - l_2^2 + l_3^2 - 2l_o l_1 \cos\theta_l \tag{22}$$

Letting $\tau = \tan(\phi_l/2)$, and making use of double-angle trigonometric identities yields:

$$\sin\phi_l = \frac{2\tau}{1+\tau^2} \tag{23}$$

$$\cos\phi_l = \frac{1-\tau^2}{1+\tau^2} \tag{24}$$

Substituting Eqs. (23) and (24) into Eq. (19) yields a quadratic equation in τ for a given crank angle θ_l:

$$(K_3 - K_2)\tau^2 + 2K_1\tau + (K_3 + K_2) = 0 \tag{25}$$

from which one can readily solve for the rocker-arm angle ϕ_l via:

$$\phi_l = 2 \cdot \arctan2\left(\frac{-K_1 \pm \sqrt{K_1^2 - K_3^2 + K_2^2}}{K_3 - K_2}\right) \tag{26}$$

where arctan2 denotes the 4-quadrant arc-tangent function that is dependent upon the signs of the numerator and denominator. The coupler angle α_l can then be solved by dividing Eq. (17) by Eq. (18):

$$\alpha_l = \arctan2\left(\frac{l_3\sin\phi_l - l_1\sin\theta_l}{l_o + l_3\cos\phi_l - l_1\cos\theta_l}\right) \tag{27}$$

Hence, $\alpha_l(\theta_l)$ and $\phi_l(\theta_l)$ can effectively be written as functions of θ_l.

The relationships between the crank angular velocity $\dot{\theta}_l$, and the dependent angular velocities, $\dot{\alpha}_l$ and $\dot{\phi}_l$, can also be determined. Differentiating the loop closure equations in Eqs. (15) and (16) with respect to time yields:

$$-l_1\dot{\theta}_l \sin\theta_l - l_2\dot{\alpha}_l \sin\alpha_l + l_3\dot{\phi}_l \sin\phi_l = 0 \tag{28}$$

$$l_1\dot{\theta}_l \cos\theta_l + l_2\dot{\alpha}_l \cos\alpha_l - l_3\dot{\phi}_l \cos\phi_l = 0 \tag{29}$$

Equations (28) and (29) can be conveniently written as a linear algebra problem that can be solved for $\dot{\alpha}_l$ and $\dot{\phi}_l$ via Cramer's rule yielding:

$$\dot{\alpha}_l = \frac{l_1}{l_2}\frac{\sin(\phi_l - \theta_l)}{\sin(\alpha_l - \phi_l)}\dot{\theta}_l \tag{30}$$

$$\dot{\phi}_l = \frac{l_1}{l_3}\frac{\sin(\alpha_l - \theta_l)}{\sin(\alpha_l - \phi_l)}\dot{\theta}_l \tag{31}$$

Since $\theta_l = \Gamma\theta$, Eqs. (30) and (31) can be written as:

$$\dot{\alpha}_l = S_1(\theta)\dot{\theta} = \frac{\partial\alpha_l}{\partial\theta}\dot{\theta} \tag{32}$$

$$\dot{\phi}_l = S_2(\theta)\dot{\theta} = \frac{\partial\phi_l}{\partial\theta}\dot{\theta} \tag{33}$$

where,

$$S_1(\theta) \triangleq \Gamma\frac{l_1}{l_2}\frac{\sin(\phi_l - \Gamma\theta)}{\sin(\alpha_l - \phi_l)} \tag{34}$$

$$S_2(\theta) \triangleq \Gamma\frac{l_1}{l_3}\frac{\sin(\alpha_l - \Gamma\theta)}{\sin(\alpha_l - \phi_l)} \tag{35}$$

Therefore, the linkage element velocities $\dot{\alpha}_l$, $\dot{\phi}_l$, and $\dot{\theta}_l$ can be written in terms of a single motion variable and its time derivative, viz. the the motor angular position θ and angular velocity $\dot{\theta}$.

2. Lagrangian of Four-Bar Linkage

The kinetic energy of the linkage elements is given by:

$$T_l = \frac{1}{2}\left[m_1\|v_{c_1}\|^2 + I_1\dot{\theta}_l^2 + m_2\|v_{c_2}\|^2 + I_2\dot{\alpha}_l^2 + m_3\|v_{c_3}\|^2 + I_3\dot{\phi}_l^2 + m_p(\|v_{p_1}\|^2 + \|v_{p_2}\|^2)\right] \tag{36}$$

where v_{c_1}, v_{c_2} and v_{c_3} are the linear velocities of the centers-of-mass of the crank, coupler, and rocker respectively; m_p is the mass of the linkage pins, and v_{p_1} and v_{p_2} are the velocities of the two pins. The center-of-mass of the crank is constant because it is formed from the final gear, which is axis-symmetric, thus $v_{c_1} = 0$ and $I_1 = J_{gn_g}$. Expanding Eq. (36) yields:

$$T_l = \frac{1}{2}\left[I_1\dot{\theta}_l^2 + m_2(l_1^2\dot{\theta}_l^2 + l_{c_2}^2\dot{\alpha}_l^2 + 2l_1l_{c_2}\cos(\theta_l - \alpha_l)\dot{\alpha}_l\dot{\theta}_l) + I_2\dot{\alpha}_l^2 + (m_3l_{c_3}^2 + I_3)\dot{\phi}_l^2 + m_p(l_1^2\dot{\theta}_l^2 + l_3^2\dot{\phi}_l^2)\right] \tag{37}$$

Collecting terms on the products of the angular velocities and substituting Eqs. (9) and (11) into Eq. (37) yields:

$$T_l = \frac{1}{2}[J_{1_l}\dot{\theta}^2 + J_{2_l}\dot{\alpha}_l^2 + J_{3_l}\dot{\phi}_l^2 + 2P_1C_1\dot{\alpha}_l\dot{\theta}] \tag{38}$$

where,

$$J_{1_l} = \Gamma^2\left[I_1 + m_2l_1^2 + m_pl_1^2\right] \tag{39}$$

$$J_{2_l} = m_2l_{c_2}^2 + I_2 \tag{40}$$

$$J_{3_l} = m_3l_{c_3}^2 + m_pl_3^2 + I_3 \tag{41}$$

$$P_1 = m_2l_1l_{c_2}\Gamma \tag{42}$$

$$C_1 = \cos(\theta_l - \alpha_l) \tag{43}$$

Note that the linkage operates in a plane that is perpendicular to the gravitational vector, thus, there is no change in potential energy of the linkage elements as the crank rotates. Hence, only kinetic energy contributes to the total Lagrangian associated with the *four-bar linkage subsystem*. Substituting Eqs. (30) and (31) into Eq. (38) yields the complete expression for the kinetic energy and Lagrangian of the linkage in terms of the motor angular velocity $\dot{\theta}$:

$$\mathcal{L}_l = T_l = \frac{1}{2}[J_{1_l} + J_{2_l} S_1^2 + J_{3_l} S_2^2 + 2P_1 C_1 S_1]\dot{\theta}^2 \tag{44}$$

D. Flexible Spar

Typical MAV ornithopters use carbon fiber components for the wing structure and thin films, such as Mylar, for the wing skin. In general, the interactions of the motor, gears, linkage, and wing are of interest. In the analysis that follows, the structural dynamics of a wing spar are considered, since the leading edge wing spar provides the primary resistance to wing bending in the stroke plane. Figure 4 shows a diagram of a four bar linkage with a flexible wing spar clamped to the end of a rocker-arm.

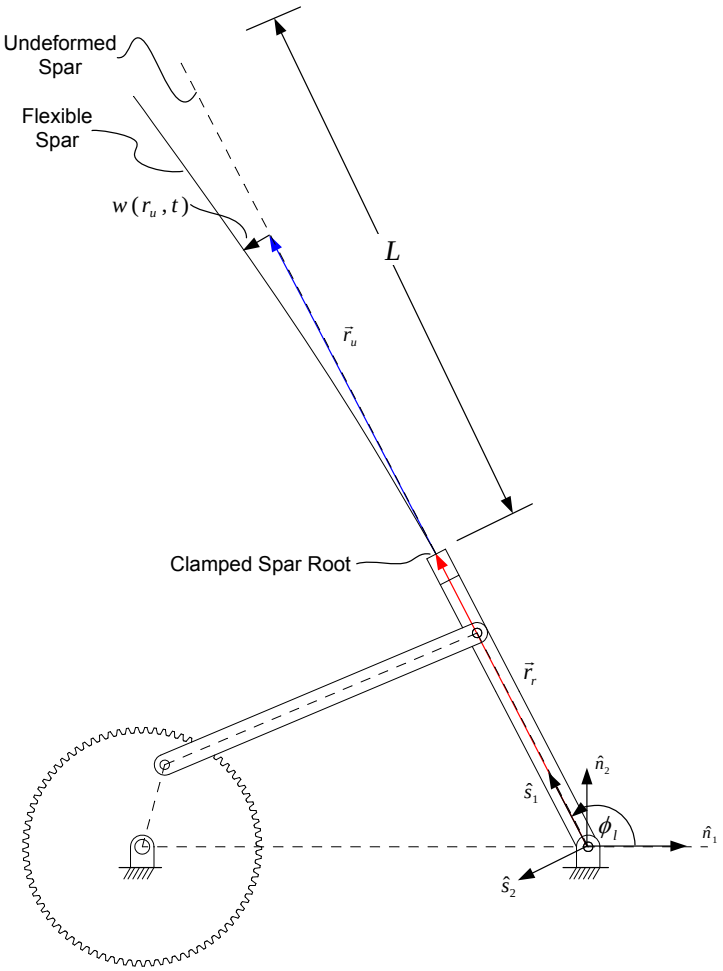

Figure 4. Flexible spar driven by rocker arm.

An inertial frame, represented by the unit vectors $\hat{n}_1, \hat{n}_2$, is fixed at the center-of-rotation of the rocker-arm. A coordinate frame that rotates with the rocker arm is denoted as $\hat{s}_1, \hat{s}_2$. A vector from the origin of frame $\hat{s}_1 - \hat{s}_2$ to the point at which the spar is clamped to the rocker arm is denoted as $\vec{r}_r$. A vector from the clamped root of the spar to an arbitrary point on the undeformed spar is denoted as $\vec{r}_u$. A vector from a point on the undeformed spar to a point on the deformed spar is denoted as $w(r_u, t)$ where $r_u \triangleq |\vec{r}_u|$. The deformation $w(r_u, t)$ is taken to be perpendicular to the undeformed spar and therefore occurs only in

the $\hat{s}_2$ direction. When viewed from the rocker-arm frame, the flexible spar appears as a cantilever beam[b]. The motion of the rocker-arm will cause the spar to deform due to bending. Euler-Bernoulli beam theory is used in the following analysis and the spar is taken to have uniform cross section and Young's modulus. The assumed modes method[27] is used to describe the deformation of the spar in the stroke plane relative to the $\hat{s}_1$ axis. The deformation is taken to be described by an infinite sum of the products of spatially dependent mode shape functions $\Phi_i(r_u)$ and temporal modal coordinates $\eta_i(t)$, i.e.:

$$w(r_u, t) = \sum_{i=1}^{\infty} \Phi_i(r_u)\eta_i(t) \tag{45}$$

where, for clamped-free boundary conditions, the ith mode shape function is given by:

$$\Phi_i(r_u) = A_i \left[a_i(\sin\beta_i r_u - \sinh\beta_i r_u) + b_i(\cos\beta_i r_u - \cosh\beta_i r_u)\right] \tag{46}$$

where,

$$a_i \triangleq (\sin\beta_i L - \sinh\beta_i L) \tag{47}$$

$$b_i \triangleq (\cos\beta_i L + \cosh\beta_i L) \tag{48}$$

and β_i is the ith solution to the frequency equation:

$$\cos\beta_i L \cosh\beta_i L = -1 \tag{49}$$

and A_i is an arbitrary constant with units of length[c]. For a cantilever beam with uniform properties along its length:

$$\beta_i^4 = \frac{\omega_i^2 \hat{m}}{E_s I_s} \tag{50}$$

where ω_i is the natural frequency of the ith bending mode, $\hat{m}$ is the mass per unit length of the beam, E_s is the Young's modulus of the spar, and I_s is the area moment of inertia of the cross section of the spar about the neutral axis.

In the analysis that follows, the *first and second bending modes* are retained in the response[d]. Hence,

$$w(r_u, t) = \Phi_1(r_u)\eta_1(t) + \Phi_2(r_u)\eta_2(t) \tag{51}$$

Solving the frequency equation for the first two bending modes yields:

$$\omega_1 = 1.875^2\sqrt{\frac{E_s I_s}{\hat{m}L^4}} \tag{52}$$

$$\omega_2 = 4.694^2\sqrt{\frac{E_s I_s}{\hat{m}L^4}} \tag{53}$$

where the constants are accurate to 4 significant figures. It is also useful to note that:

$$\beta_1 = \frac{1.875}{L} \tag{54}$$

$$\beta_2 = \frac{4.694}{L} \tag{55}$$

1. *Flexible Spar Kinetic Energy*

For convenience, define $r \triangleq r_r + r_u$. Note that r_r extends along the rigid rocker arm from the pivot point to the clamped end of the spar. From Fig. 4, one may write the position vector from the origin of the rocker arm to a point on the deformed beam as:

$$\vec{r}_p = \left[r\cos\phi_l - w\sin\phi_l\right]\hat{n}_1 + \left[r\sin\phi_l + w\cos\phi_l\right]\hat{n}_2 \tag{56}$$

[b]Note that the rocker arm angle ϕ_l remains a function of motor position θ

[c]In the literature, the arbitrary constant associated with each mode is often used to mass normalize the mode shapes

[d]For the case considered in the results section, it was found that retaining only the first bending mode yielded excellent results; nevertheless, a more general two-mode case has been considered in the analytical development

Substituting Eq. (51) yields:

$$\vec{r_p} = [r\cos\phi_l - (\Phi_1\eta_1 + \Phi_2\eta_2)\sin\phi_l]\,\hat{n}_1 + [r\sin\phi_l + (\Phi_1\eta_1 + \Phi_2\eta_2)\cos\phi_l]\,\hat{n}_2 \tag{57}$$

Differentiating Eq. (57) with respect to time yields:

$$\begin{aligned}\dot{\vec{r}}_p = &\left[-r\dot{\phi}_l\sin\phi_l - (\Phi_1\eta_1 + \Phi_2\eta_2)\dot{\phi}_l\cos\phi_l - (\Phi_1\dot{\eta}_1 + \Phi_2\dot{\eta}_2)\sin\phi_l\right]\hat{n}_1 + \\ &\left[r\dot{\phi}_l\cos\phi_l - (\Phi_1\eta_1 + \Phi_2\eta_2)\dot{\phi}_l\sin\phi_l + (\Phi_1\dot{\eta}_1 + \Phi_2\dot{\eta}_2)\cos\phi_l\right]\hat{n}_2\end{aligned} \tag{58}$$

The differential kinetic energy of an elemental beam segment on the deformable spar is given by:

$$dT_s = \frac{1}{2}\hat{m}[\dot{\vec{r}}_p \cdot \dot{\vec{r}}_p]dr \tag{59}$$

or, with some mathematical manipulation,

$$dT_s = \frac{1}{2}\hat{m}\left[r^2\dot{\phi}_l^2 + (\Phi_1\eta_1 + \Phi_2\eta_2)^2\dot{\phi}_l^2 + (\Phi_1\dot{\eta}_1 + \Phi_2\dot{\eta}_2)^2 + 2r\dot{\phi}_l(\Phi_1\dot{\eta}_1 + \Phi_2\dot{\eta}_2)\right]dr \tag{60}$$

Integrating Eq. (60) from the root to the tip of the spar yields:

$$T_s = \frac{1}{2}\hat{m}\int_{r_r}^{r_r+L}\left[r^2\dot{\phi}_l^2 + (\Phi_1\eta_1 + \Phi_2\eta_2)^2\dot{\phi}_l^2 + (\Phi_1\dot{\eta}_1 + \Phi_2\dot{\eta}_2)^2 + 2r\dot{\phi}_l(\Phi_1\dot{\eta}_1 + \Phi_2\dot{\eta}_2)\right]dr \tag{61}$$

or

$$T_s = \frac{1}{2}\hat{m}\int_0^L\left[(r_r + r_u)^2\dot{\phi}_l^2 + (\Phi_1\eta_1 + \Phi_2\eta_2)^2\dot{\phi}_l^2 + (\Phi_1\dot{\eta}_1 + \Phi_2\dot{\eta}_2)^2 + 2(r_r + r_u)\dot{\phi}_l(\Phi_1\dot{\eta}_1 + \Phi_2\dot{\eta}_2)\right]dr_u \tag{62}$$

Recall that the shape functions, Φ_i, are functions of r_u only, and that ϕ_l, η_1 and η_2 are functions of time and do not vary with r_u. Carrying out the integration of Eq. (62) yields:

$$T_s = \frac{1}{2}\hat{m}\left[c_1\dot{\phi}_l^2 + c_2(\dot{\phi}_l^2\eta_1^2 + \dot{\eta}_1^2) + 2c_4\dot{\phi}_l\dot{\eta}_1 + 2c_6(\eta_1\eta_2\dot{\phi}_l^2 + \dot{\eta}_1\dot{\eta}_2) + c_7(\dot{\phi}_l^2\eta_2^2 + \dot{\eta}_2^2) + 2c_8\dot{\phi}_l\dot{\eta}_2\right] \tag{63}$$

where:

$$c_1 = \int_0^L (r_r + r_u)^2 dr_u = \frac{L^3}{3} + L^2 r_r + L r_r^2 \tag{64}$$

$$c_2 = \int_0^L \Phi_1^2 dr_u = 9.226L \tag{65}$$

$$c_4 = \int_0^L (r_r + r_u)\Phi_1 dr_u = -L(1.728L + 2.378r_r) \tag{66}$$

$$c_6 = \int_0^L \Phi_1\Phi_2 dr_u = 0 \tag{67}$$

$$c_7 = \int_0^L \Phi_2^2 dr_u = 2984.480L \tag{68}$$

$$c_8 = \int_0^L (r_r + r_u)\Phi_2 dr_u = -L(4.959L + 23.707r_r) \tag{69}$$

Note that the decimal constants in c_2 and c_7 have units of length squared, while the decimal constants in c_4 and c_8 have units of length, and c_6 is 0 since the mode shapes are orthogonal. Substituting Eq. (35) and Eq. (67) into Eq. (63) yields:

$$T_s = \frac{1}{2}\hat{m}\left[c_1 S_2^2\dot{\theta}^2 + c_2(S_2^2\dot{\theta}^2\eta_1^2 + \dot{\eta}_1^2) + 2c_4 S_2\dot{\theta}\dot{\eta}_1 + c_7(S_2^2\dot{\theta}^2\eta_2^2 + \dot{\eta}_2^2) + 2c_8 S_2\dot{\theta}\dot{\eta}_2\right] \tag{70}$$

The kinetic energy of the spar is now written in terms of the three motion variables of interest, viz., θ, η_1, η_2, and their derivatives.

2. Flexible Spar Strain Energy

By definition, the strain energy due to bending of an Euler-Bernoulli beam is given by[28] :

$$V_s = \frac{1}{2} E_s I_s \int_0^L w''(r_u, t)^2 dr_u \tag{71}$$

Retaining only the first two bending modes and setting the arbitrary constant, A_i, of Eq. (46) to unity, the second spatial derivative of the deformation becomes:

$$\begin{gathered} w''(r_u, t) = \beta_1^2 \left[-a_1(\cos\beta_1 r_u + \cosh\beta_1 r_u) - b_1(\sin\beta_1 r_u + \sinh\beta_1 r_u) \right] \eta_1 + \\ \beta_2^2 \left[-a_2(\cos\beta_2 r_u f + \cosh\beta_2 r_u) - b_2(\sin\beta_2 r_u + \sinh\beta_2 r_u) \right] \eta_2 \end{gathered} \tag{72}$$

Squaring Eq. (72) and evaluating Eq. (71) yields the strain energy of the spar due to bending deformation from the first two bending modes:

$$V_s = \frac{1}{2} E_s I_s \left[c_5 \eta_1^2 + c_{10} \eta_2^2 \right] \tag{73}$$

where,

$$c_5 = \int_0^L \Phi_1^{2\prime\prime} dr_u = \frac{114.082}{L^3} \tag{74}$$

$$c_{10} = \int_0^L \Phi_2^{2\prime\prime} dr_u = \frac{1.449 \times 10^6}{L^3} \tag{75}$$

Integrals of the products of the two mode shapes are zero because of orthogonality. The decimal constants in c_5 and c_{10} have units of length squared. The contribution of the *flexible spar subsystem* to the Lagrangian is:

$$\mathcal{L}_s = T_s - V_s \tag{76}$$

or

$$\mathcal{L}_s = \frac{1}{2}\hat{m} \left[c_1 S_2^2 \dot{\theta}^2 + c_2(S_2^2 \dot{\theta}^2 \eta_1^2 + \dot{\eta}_1^2) + 2c_4 S_2 \dot{\theta}\dot{\eta}_1 + c_7(S_2^2 \dot{\theta}^2 \eta_2^2 + \dot{\eta}_2^2) + 2c_8 S_2 \dot{\theta}\dot{\eta}_2 \right] - E_s I_s \left[c_5 \eta_1^2 + c_{10} \eta_2^2 \right] \tag{77}$$

IV. Equations-of-Motion

In Section III, the Lagrangian contribution of each subsystem was evaluated. The full equations-of-motion can now be derived using Lagrange's equation:

$$\frac{d}{dt}\left(\frac{\partial \mathcal{L}}{\partial \dot{q}_i}\right) - \frac{\partial \mathcal{L}}{\partial q_i} = Q \tag{78}$$

where q_i represents the i$^t h$ generalized displacement coordinate, and Q_i the corresponding generalized forces derived from the principle of virtual work.

For the system under consideration, there are 3 generalized coordinates, namely, θ, η_1, and η_2. Hence, three coupled ordinary differential equation-of-motions are derived. The Lagrangian of the entire system can be obtained by summing Eqs. (8), (12), (44), and (77):

$$\mathcal{L} = \mathcal{L}_m + \mathcal{L}_g + \mathcal{L}_l + \mathcal{L}_s \tag{79}$$

While this paper studies a system where a DC motor drives a single gear train and four-bar linkage assembled with a flexible spar attached to the rocker arm, it is straight-forward to extend the formulation to account for systems with additional elements. For instance, it is common for ornithopters to use a single motor to drive two linkage-spar assemblies, as presented by Doman and Regisford,[9] or a single linkage assembly to drive two spars. For such cases, let n_l be the number of linkage assemblies and n_s be the number of spars attached to the linkages. Assuming that only identical copies of such elements are added to the system, the more general Lagrangian can be written as:

$$\mathcal{L} = \mathcal{L}_m + \mathcal{L}_g + n_l \mathcal{L}_l + n_s \mathcal{L}_s \tag{80}$$

The remainder of this section evaluates the inertial and Coriolis/centrifugal terms associated with the left-hand side of Lagrange's equation in Eq. (78). In the interest of establishing a general set of equations in which components may be added or subtracted from the system, we note that the derivative of a sum is equal to the sum of the derivatives, thus Lagrange's equation can be evaluated for each component, and the results can be added together to create the full equations of motion. One can derive the more general cases using the Lagrangian shown in Eq. (80).

A. DC Motor

Referring to Eq. (8), it can be seen that the Lagrangian associated with the motor is a function of the single motion variable $\dot{\theta}$. Hence, it is straight-forward to show that the contribution of the motor to the equation of motion associated with the rigid body degree-of-freedom is given by:

$$\frac{d}{dt}\left(\frac{\partial \mathcal{L}_m}{\partial \dot{\theta}}\right) = J_a \ddot{\theta} \tag{81}$$

The motor also contributes to the nonconservative input torque:

$$Q_{m_\theta} = \tau_\theta \tag{82}$$

Recall that τ_θ includes the effects of the voltage applied to the armature and the back EMF damping effect, which is a function of the motion variable $\dot{\theta}$.

B. Gear Train

The Lagrangian expression for the gear train in Eq. (12), is a function of $\dot{\theta}$ only. Hence, the contribution of the gear train to the equation of motion of motion associated with the rigid-body degree-of-freedom can be evaluated as:

$$\frac{d}{dt}\left(\frac{\partial \mathcal{L}_g}{\partial \dot{\theta}}\right) = \left(\sum_{k=0}^{n_g-1} \prod_{j=1}^{k} J_{gk} G_j^2\right) \ddot{\theta} \tag{83}$$

For the test article considered in this manuscript, Eq. (13) yields:

$$\frac{d}{dt}\left(\frac{\partial \mathcal{L}_g}{\partial \dot{\theta}}\right) = J_{g_\theta} \ddot{\theta} \tag{84}$$

where

$$J_{g_\theta} = \left(J_{g0} + J'_{g1} G_1^2\right) \tag{85}$$

in which the mass moment of inertia of the encoder is also included.

C. Four-Bar Linkage

The Lagrangian of the four-bar linkage $\mathcal{L}_l$ is completely written in terms of θ and $\dot{\theta}$ as shown in Eq. (44); however, due to the highly nonlinear couplings between the angular quantities, care must be taken to ensure that all dependencies are considered when evaluating the derivatives associated with Lagrange's equation. The contribution of the four-bar linkage to the equation of motion associated with the rigid body degree-of-freedom is given by:

$$\frac{d}{dt}\left(\frac{\partial \mathcal{L}_l}{\partial \dot{\theta}}\right) - \frac{\partial \mathcal{L}_l}{\partial \theta} \tag{86}$$

Examination of Eqs. (34) and (35), and (38) reveals that S_1, S_2, and C_1 are functions of all of the angular position variables associated with the four-bar linkage, which can be expressed in terms of the time dependent motor angular position, i.e.:

$$\begin{aligned} &S_1\left(\theta(t), \alpha_l(\theta(t)), \phi_l(\theta(t))\right) \\ &S_2\left(\theta(t), \alpha_l(\theta(t)), \phi_l(\theta(t))\right) \\ &C_1\left(\theta(t), \alpha_l(\theta(t))\right) \end{aligned} \tag{87}$$

For brevity, in the subsequent development the dependence of these terms upon $\theta(t)$ is implied rather than explicitly written. In order to evaluate Eq. (86), it is necessary to compute the time derivatives of these functions. Application of the multi-variable chain rule yields:

$$\frac{dS_1}{dt} = \tilde{S}_1 \frac{d\theta}{dt} \tag{88}$$

$$\frac{dS_2}{dt} = \tilde{S}_2 \frac{d\theta}{dt} \tag{89}$$

$$\frac{dC_1}{dt} = \tilde{C}_1 \frac{d\theta}{dt} \tag{90}$$

where,

$$\tilde{S}_1 = \left[\frac{\partial S_1}{\partial \theta} + \frac{\partial S_1}{\partial \alpha_l} \frac{\partial \alpha_l}{\partial \theta} + \frac{\partial S_1}{\partial \phi_l} \frac{\partial \phi_l}{\partial \theta} \right] \tag{91}$$

$$\tilde{S}_2 = \left[\frac{\partial S_2}{\partial \theta} + \frac{\partial S_2}{\partial \alpha_l} \frac{\partial \alpha_l}{\partial \theta} + \frac{\partial S_2}{\partial \phi_l} \frac{\partial \phi_l}{\partial \theta} \right] \tag{92}$$

$$\tilde{C}_1 = \left[\frac{\partial C_1}{\partial \theta} + \frac{\partial C_1}{\partial \alpha} \frac{\partial \alpha_l}{\partial \theta} \right] \tag{93}$$

However, from Eqs. (34) and (35), it readily follows that:

$$\tilde{S}_1 = \left[\frac{\partial S_1}{\partial \theta} + \frac{\partial S_1}{\partial \alpha_l} S_1 + \frac{\partial S_1}{\partial \phi_l} S_2 \right] \tag{94}$$

$$\tilde{S}_2 = \left[\frac{\partial S_2}{\partial \theta} + \frac{\partial S_2}{\partial \alpha_l} S_1 + \frac{\partial S_2}{\partial \phi_l} S_2 \right] \tag{95}$$

$$\tilde{C}_1 = \left[\frac{\partial C_1}{\partial \theta} + \frac{\partial C_1}{\partial \alpha_l} S_1 \right] \tag{96}$$

where the full expressions for the individual partial derivatives can be found in the Appendix. Hence, evaluating each of the terms in Eq. (86) yields:

$$\frac{d}{dt}\left(\frac{\partial \mathcal{L}_l}{\partial \dot{\theta}} \right) = J_{l_\theta} \ddot{\theta} + 2\sigma_{l_\theta} \dot{\theta}^2 \tag{97}$$

$$\frac{\partial \mathcal{L}_l}{\partial \theta} = \sigma_{l_\theta} \dot{\theta}^2 \tag{98}$$

where

$$J_{l_\theta} = \left(J_{1_l} + J_{2_l} S_1^2 + J_{3_l} S_2^2 + 2P_1 C_1 S_1 \right) \tag{99}$$

$$\sigma_{l_\theta} = \left((P_1 C_1 + J_{2_l} S_1) \tilde{S}_1 + J_{3_l} S_2 \tilde{S}_2 + P_1 S_1 \tilde{C}_1 \right) \tag{100}$$

Finally, Eq. (86) becomes:

$$\frac{d}{dt}\left(\frac{\partial \mathcal{L}_l}{\partial \dot{\theta}} \right) - \frac{\partial \mathcal{L}_l}{\partial \theta} = J_{l_\theta} \ddot{\theta} + \sigma_{l_\theta} \dot{\theta}^2 \tag{101}$$

D. Flexible Spar

For the Lagrangian of the flexible spar in Eq. (77), note that all three generalized coordinates, θ, η_1 and η_2, are involved. Hence, the flexible spar will contribute to three equations of motion. Evaluation of Lagrange's equation for the coordinate θ, yields:

$$\frac{d}{dt}\left(\frac{\partial \mathcal{L}_s}{\partial \dot{\theta}} \right) - \frac{\partial \mathcal{L}_s}{\partial \theta} = J_{s_\theta}^{\theta} \ddot{\theta} + J_{s_\theta}^{\eta_1} \ddot{\eta}_1 + J_{s_\theta}^{\eta_2} \ddot{\eta}_2 + \sigma_{s_\theta} \dot{\theta}^2 + \kappa_{s_\theta} \tag{102}$$

where

$$J^{\theta}_{s_\theta} = \hat{m} S_2^2 (c_1 + c_2 \eta_1^2 + c_7 \eta_2^2) \tag{103}$$
$$J^{\eta_1}_{s_\theta} = \hat{m} c_4 S_2 \tag{104}$$
$$J^{\eta_2}_{s_\theta} = \hat{m} c_8 S_2 \tag{105}$$
$$\sigma_{s_\theta} = \hat{m} S_2 \tilde{S}_2 (c_1 + c_2 \eta_1^2 + c_7 \eta_2^2) \tag{106}$$
$$\kappa_{s_\theta} = 2 \hat{m} S_2^2 \dot{\theta} (c_2 \dot{\eta}_1 \eta_1 + c_7 \dot{\eta}_2 \eta_2) \tag{107}$$

Evaluation of Lagrange's equation for the coordinate η_1, yields:

$$\frac{d}{dt}\left(\frac{\partial \mathcal{L}_s}{\partial \dot{\eta}_1}\right) - \frac{\partial \mathcal{L}_s}{\partial \eta_1} = J^{\theta}_{s_{\eta_1}} \ddot{\theta} + J^{\eta_1}_{s_{\eta_1}} \ddot{\eta}_1 + \sigma_{s_{\eta_1}} \dot{\theta}^2 + \kappa_{s_{\eta_1}} \tag{108}$$

where,

$$J^{\theta}_{s_{\eta_1}} = \hat{m} c_4 S_2 \tag{109}$$
$$J^{\eta_1}_{s_{\eta_1}} = \hat{m} c_2 \tag{110}$$
$$\sigma_{s_{\eta_1}} = \hat{m} (c_4 \tilde{S}_2 - c_2 S_2^2 \eta_1) \tag{111}$$
$$\kappa_{s_{\eta_1}} = E_s I_s c_5 \eta_1 \tag{112}$$

Evaluation of Lagrange's equation for the coordinate η_2, yields:

$$\frac{d}{dt}\left(\frac{\partial \mathcal{L}_s}{\partial \dot{\eta}_2}\right) - \frac{\partial \mathcal{L}_s}{\partial \eta_2} = J^{\theta}_{s_{\eta_2}} \ddot{\theta} + J^{\eta_2}_{s_{\eta_2}} \ddot{\eta}_2 + \sigma_{s_{\eta_2}} \dot{\theta}^2 + \kappa_{s_{\eta_2}} \tag{113}$$

where,

$$J^{\theta}_{s_{\eta_2}} = \hat{m} c_8 S_2 \tag{114}$$
$$J^{\eta_1}_{s_{\eta_2}} = \hat{m} c_7 \tag{115}$$
$$\sigma_{s_{\eta_2}} = \hat{m} (c_8 \tilde{S}_2 - c_7 S_2^2 \eta_2) \tag{116}$$
$$\kappa_{s_{\eta_2}} = E_s I_s c_{10} \eta_2 \tag{117}$$

E. Complete Equations of Motion

Finally, the complete equations of motion can be written as:

$$\begin{bmatrix} \left(J_a + J_{g_\theta} + J_{l_\theta}(\theta) + J^{\theta}_{s_\theta}(\theta)\right) & J^{\eta_1}_{s_\theta}(\theta) & J^{\eta_2}_{s_\theta}(\theta) \\ J^{\theta}_{s_{\eta_1}}(\theta) & J^{\eta_1}_{s_{\eta_1}} & 0 \\ J^{\theta}_{s_{\eta_2}}(\theta) & 0 & J^{\eta_2}_{s_{\eta_2}} \end{bmatrix} \begin{bmatrix} \ddot{\theta} \\ \ddot{\eta}_1 \\ \ddot{\eta}_2 \end{bmatrix} + \begin{bmatrix} \sigma_{l_\theta}(\theta) + \sigma_{s_\theta}(\theta, \eta_1, \eta_2) \\ \sigma_{s_{\eta_1}}(\theta, \eta_1) \\ \sigma_{s_{\eta_2}}(\theta, \eta_2) \end{bmatrix} \dot{\theta}^2 + \tag{118}$$
$$\begin{bmatrix} \kappa_{s_\theta}(\theta, \dot{\theta}, \eta_1, \dot{\eta}_1, \eta_2, \dot{\eta}_2) \\ \kappa_{s_{\eta_1}}(\eta_1) \\ \kappa_{s_{\eta_2}}(\eta_2) \end{bmatrix} = \begin{bmatrix} Q_{m_\theta}(e_a) + Q_{l_\theta}(\dot{\theta}) + Q_{d_\theta}(\theta, \dot{\theta}, \eta_1, \dot{\eta}_1, \eta_2, \dot{\eta}_2) \\ Q_{s_{\eta_1}}(\dot{\eta}_1) + Q_{d_{\eta_1}}(\theta, \dot{\theta}, \eta_1, \dot{\eta}_1, \eta_2, \dot{\eta}_2) \\ Q_{s_{\eta_2}}(\dot{\eta}_2) + Q_{d_{\eta_2}}(\theta, \dot{\theta}, \eta_1, \dot{\eta}_1, \eta_2, \dot{\eta}_2) \end{bmatrix}$$

which can be integrated using numerical methods. The explicit dependence of the inertial, Coriolis, and generalized force terms upon the state variables is shown to highlight the extensive coupling present in such a system. The forcing term that drives these equations is the armature voltage e_a. Thus, these equations can be used to predict how the system will behave when a constant or time varying voltage is applied to the motor armature. These equations provide a powerful analysis tool for MAV system designers. They could also be used as a model to support the design of mechanism control laws that have the potential to improve the behavior of wing beat motion over what could be achieved by applying a constant voltage to the motor.

There are a number of generalized forces that act upon the system such as a velocity dependent frictional/back-EMF term associated with the θ coordinate, which can be written as $Q_{l_\theta} = B_\theta \dot{\theta}$, the damping within the flexible spar that is proportional to the modal coordinate rates $Q_{s_{\eta_1}} = 2\zeta_1 \omega_1 \dot{\eta}_1$, $Q_{s_{\eta_2}} = 2\zeta_2 \omega_2 \dot{\eta}_2$, and the aerodynamic drag of the spar that influences each degree of freedom via Q_{d_θ},$Q_{d_{\eta 1}}$, and $Q_{d_{\eta 2}}$. Methods for estimating each of these generalized forces will be discussed in the next two sections.

V. Estimation of Generalized Forces

The analytical method presented thus far yields the form of the governing dynamical equations. There are several constants that are device dependent and can only be determined experimentally. With respect to the DC motor, the motor torque constant K_T, back-EMF constant K_b, and armature resistance R_a must be determined experimentally or be provided by the motor manufacturer. The friction characteristics of the gear train and linkage as well as the modal damping of the spar structural modes must also be determined from experiments. A process for the estimating each of these terms is be presented below.

A. Motor Drive Torque

The generalized force, Q_{m_θ}, is the motor drive torque, which is given by:

$$Q_{m_\theta} = \frac{K_T}{R_a} e_a \tag{119}$$

The motor torque constant K_T and armature resistance R_a must be measured, or supplied by the motor manufacturer. A description of how to estimate the motor torque constant from experiments is provided below. The armature voltage e_a forms the external input into the equations of motion.

B. Generalized Frictional Force

The overall generalized friction force Q_{l_θ} is a lumped parameter that includes the effects of back-EMF and viscous friction in the gear train, linkage and the motor itself.

$$Q_{l_\theta} = B_\theta \dot{\theta} \tag{120}$$

where

$$B_\theta = -\left(\frac{K_T K_B}{R_m} + b \right) \tag{121}$$

A description of how the terms in Eq. 120 were measured follows.

1. Determination of Motor Characteristics

The important physical properties of most small motors being used in flapping wing MAV prototypes are not well characterized by their manufacturer. This is because many of these motors are used to power toys or pager motors, and such detailed design information is not required for those applications. A method for extracting estimates of the required motor parameters is presented.

First, consider the problem of extracting of the back-EMF constant of the motor. By substituting Eq. 3 into Eq. 5, one can solve for K_b:

$$K_b = \frac{1}{\dot{\theta}} (e_a - R_a i_a) \tag{122}$$

Most of the parameters on the right hand side of the equation are measurable in the laboratory using a digital multimeter. The measurement of $\dot{\theta}$ can be performed using a strobe light, an optical encoder, or a visual image correlation system. Alternatively, Eq. 3 can be used directly if an active drive motor is coupled to an optical encoder and to the test motor via an idler gear. The output voltage e_b generated by the test motor can be measured, while the period of the pulse train generated by the optical encoder can be used to determine the motor speed. Each of the methods described above have been used by the authors and have been found to produce nearly identical estimates of the back-EMF constant on a 7mm pager motor manufactured by Super Slicks. The motor used in the test article is known in hobbyist circles as a Red Super Slicks motor and has an armature resistance of 2.3 Ohms.

The estimation of the torque constant K_T followed the method outlined by the Didel company[e]. A pinion was mounted on the motor shaft. An arm with a splined hole near one end was fitted over the pinion. A point on the opposite end of the arm was oriented perpendicular to the longitudinal axis of the arm. The motor was mounted securely to a laboratory bench and the point of the arm was placed on a scale with a 0.1 g resolution. Multiplying the moment arm by the force measurement yielded the stall torque. The torque

[e] http://www.didel.com/microkit/moteurs/Motors.html

constant was then be determined from Eq. 2. The resulting mean estimate for the torque constant was 6774 dyne-cm/amp with a standard deviation of 619 dyne-cm/amp. The high standard deviation was attributed to the low resolution of the scale used in the test.

2. Determination of Mechanism Friction

An initial estimate of the friction characteristics of the mechanism was obtained by measuring the steady-state speed of the motor, gear train, and linkage and the current flowing through the motor. Note that the wing spar was not attached to the mechanism during this test. A viscous friction model was used to describe the effect of all sources of mechanical friction within the subsystem, viz.,

$$\tau_f = -b\dot{\theta} \tag{123}$$

With knowledge of the motor torque constant, back EMF constant, steady state current, and steady state speed, the viscous friction coefficient was estimated from:

$$b = \frac{-K_T i_a}{\dot{\theta}_{ss}} - \frac{K_T K_b}{R} \tag{124}$$

where $\dot{\theta}_{ss}$ represents the steady state velocity of the motor. In the work presented here, the initial estimate of the viscous friction coefficient was obtained from experimental data from a mechanism-only test. The final adjustment of the coefficient was performed by comparing simulation time histories of crank speed to experimental measurements of crank speed using an optical encoder. It was found that the viscous friction coefficient that caused the spar stroke periods of the simulation to match those observed in the experiment was $b = 0.525$ dyne-cm/(rad/sec). It should be noted that this parameter, is very sensitive to the method of construction of the overall device. For example, friction produced by the linkage rivets or pins is related to the skill of the builder who must carefully deform the heads of the rivets to ensure planar motion of the linkage without producing excessive friction.

C. Determination of Modal Characteristics of the Spar

An estimate of the modal damping of a spar or wing structure is not normally available. A test was conducted to estimate the modal damping of the first bending mode the spar used in the experiment. The spar under consideration was a carbon fiber rod that the manufacturer markets as an "0.037 inch diameter" rod. The rod was cut to 13 cm in length. An infrared non-contact proximity sensor, consisting of an LED and photo transistor, was used measure the deflection of a point on the spar, while the root was clamped. The spar was plucked and the response was recorded at a 20 KHz sampling rate. The damping was estimated by using the well known logarithmic decrement technique. The undamped natural frequency was also estimated from the response. The magnitude of the initial tip displacement was purposely small, i.e. < 1 cm, in order to minimize the impact of aerodynamic drag upon the damping estimate. The measurement of the spar displacement in this test was limited to sensor voltage output, since the measurement of frequency and damping is not dependent upon the actual physical units of displacement, e.g. cm.

Some important observations were made while conducting the test. First, commercially available carbon fiber rod does not have a circular cross section. The cross section is best described as an oval, rather than a "0.037 inch rod" with a circular cross section. The cross section measurements varied by +/- .002 inches (+/- .005 cm). This means that "pluck" tests must be conducted with care, since an initial deformation that is not aligned with a principal axis will produce transverse vibrations along two axes, making it difficult for a non-contacting proximity sensor to accurately measure the time history of the displacement, which is required for the application of the log decrement method. The best results were obtained when the initial deformation was aligned with a principal axis. The response, as measured by the non-contact proximity sensor, was band-pass filtered with break frequencies 2 times lower and 2 times higher than the theoretical estimate of the first bending mode frequency for a spar with a circular cross section. The power spectral density of the filtered response was used to estimate the actual first bending mode frequency.

Classical beam theory estimates the natural frequency of the first bending mode of a cantilever beam to be given by Eq. 52. In order to estimate the frequency of the first bending mode of the spar from Eq. 52, one must use estimates of the following spar properties: Young's modulus, cross sectional area moment of inertia , mass per unit length, and length. The mass of the spar was determined to the nearest 1 mg on a

precision scale and the length of the rod was measured to the nearest .25 mm using a digital caliper. The mass per unit length of the spar was determined to be $\hat{m} = 0.01085$ g/cm. Using the above information and the manufacturer's specifications for $E_s = 1.227 \times 10^{12}$ dynes/cm^2, as well as the assumption that the cross section of the rod is circular, the idealized first bending mode frequency can be computed to be $\omega_{1_{theory}} = 432.88$ rad/sec. Since the product $E_s I_s$ had a higher degree of uncertainty than the spar mass and length, the measured first bending mode frequency obtained from the peak of the power spectral density was used to estimate the uncertain product. The power spectral density of the band-pass filtered tip deflection time history showed that the natural frequency of the first bending mode was located at 422.79 rad/sec. For a uniform circular cross section of an 0.037 inch (.09398 cm) round rod with an area moment of inertia about the neutral axis of $I_s = 3.83 \times 10^{-6}$cm^4 , the value of Young's modulus that matches the observed natural frequency is given by $E_s = 1.1704 \times 10^{12}$ dyne/cm^2, which is slightly lower than the manufacturer's specification. The lower frequency is most likely due to the departure from the ideal circular cross section of the rod. Indeed, beam theory predicts variations of up to $\pm$ 5% in first bending mode frequency for a rod with an elliptical cross section where the major and minor axes vary by $\pm$ .005 cm from a nominal .09398 cm (.037 inch) diameter circular cross section. The damping ratio for the first bending mode based upon the analysis using the log decrement method was found be $\zeta_1 = .0025$; the damping ratio for the second bending mode was assumed to be the same as for the first.

D. Aerodynamic Drag Forces

The standard definition for the generalized forces used in Lagrange's equations is given by:[29]

$$Q_i = \sum_{j=1} F_j \frac{\partial x_j}{\partial q_i} \tag{125}$$

where Q_i is the ith generalized force, F_j is the jth component of the external force applied to the system, q_i is the ith generalized coordinate, and $\frac{\partial x_j}{\partial q_i}$ is the jth component of the partial derivative of the position vector to the point of application of the force with respect to the ith generalized coordinate. For the derivation of the generalized forces acting on the flexible spar, the differential contribution to the generalized forces is first calculated. Then the differential contributions to the generalized forces are integrated to obtain generalized forces as a function of the angular position of the motor and the flexible modal coordinates. The derivation that follows assumes that the only external force applied to the system is due to the aerodynamic drag acting on the flexible spar and that the first two modal coordinates accurately represent the deformation. The flexible spar is modeled as a cylinder and a blade element model is used to determine the aerodynamic drag. As standard when using the blade element method, the drag over the cylinder is modeled using a rectangle with dimensions equal to the cylinder's length and diameter. Thus, the replacement area lies in the $s_1 - s_3$ plane. Blade element theory states:[30]

$$dF_D = \frac{1}{2} \rho C_d V_\infty^2 \, dA \tag{126}$$

where V_∞ is the magnitude of the velocity of a point on the representative area once it has been resolved into components that lie in the plane of the blade element. dA is the differential area over which the dynamic pressure acts. Thus $dA = dr_u \, dz_s$. It is convenient to describe the aerodynamic force in a frame that defines the blade elements. The definition of each blade element along the spar should remain constant in the coordinate frames in which they are expressed. Thus at each point in the representative area a frame can be defined that deforms along with the spar. This deformed frame is related to the frame associated with the undeformed motion of the spar through a single axis rotation. The deformation of the spar is described in Eq. 45. The angle that defines the relationship between the s-frame and the deformed d-frame is described by taking the spatial derivative of Eq. 45 with respect to the r_u variable. Thus,

$$w'(r_u, t) = \sum_{i=1}^{\infty} \Phi_i'(r_u) \eta_i(t) \tag{127}$$

As the present analysis assumes that only two modes are retained,

$$w'(r_u, t) = \Phi_1'(r_u) \eta_1(t) + \Phi_2'(r_u) \eta_2(t) \tag{128}$$

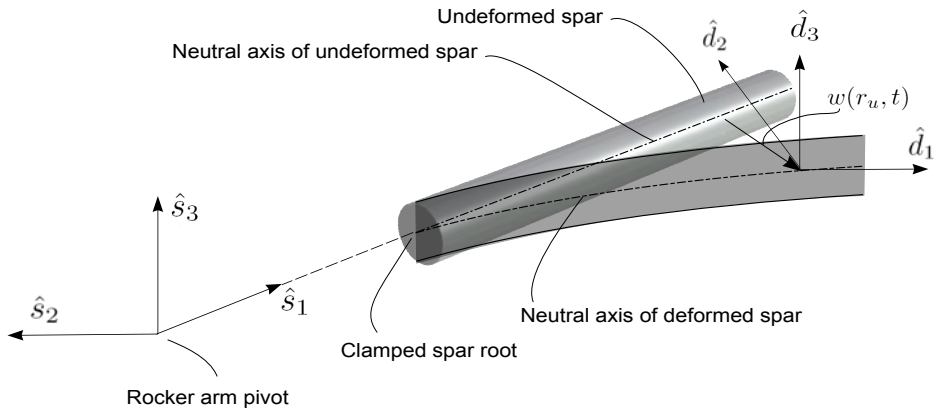

Figure 5. Coordinate frames associated with undeformed and deformed spar.

$$\begin{Bmatrix} \hat{s}_1 \\ \hat{s}_2 \\ \hat{s}_3 \end{Bmatrix} = \begin{bmatrix} \cos w'(r_u,t) & -\sin w'(r_u,t) & 0 \\ \sin w'(r_u,t) & \cos w'(r_u,t) & 0 \\ 0 & 0 & 1 \end{bmatrix} \begin{Bmatrix} \hat{d}_1 \\ \hat{d}_2 \\ \hat{d}_3 \end{Bmatrix} \tag{129}$$

The drag force acts in opposition to the direction of the velocity defined in the plane of the blade element. Thus, the differential force vector is written in the inertial frame as:

$$\begin{aligned} d\vec{F}_d &= \frac{1}{2}\rho C_d V_\infty^2 \, dA \left(-\frac{\vec{V}_\infty}{||\vec{V}_\infty||} \right) \\ &= \frac{1}{2}\rho C_d V_\infty \left(-\vec{V}_\infty \right) \, dA \end{aligned} \tag{130}$$

To define $\vec{V}_\infty$, begin with the definition of the velocity of the point written in terms of the deformed frame:

$$\begin{aligned} \vec{v}_{pr}^{\,d} = &\Big(-\left(\Phi_1(r_u)\eta_1(t) + \Phi_2(r_u)\eta_2(t)\right)\dot{\phi}_l \cos w'(r_u,t) + r\dot{\phi}\sin w'(r_u,t) + \left(\Phi_1(r_u)\dot{\eta}_1(t) + \Phi_2(r_u)\dot{\eta}_2(t)\right)\sin w'(r_u,t) \Big)\hat{d}_1 \\ &\Big(\left(\Phi_1(r_u)\eta_1(t) + \Phi_2(r_u)\eta_2(t)\right)\dot{\phi}_l \sin w'(r_u,t) + r\dot{\phi}\cos w'(r_u,t) + \left(\Phi_1(r_u)\dot{\eta}_1(t) + \Phi_2(r_u)\dot{\eta}_2(t)\right)\cos w'(r_u,t) \Big)\hat{d}_2 \end{aligned} \tag{131}$$

As the blade element lies in the $\hat{d}_2 - \hat{d}_3$ plane, $\vec{V}_\infty^{\,d}$ is defined by ignoring the $\hat{d}_1$ component of $\vec{v}_{pr}^{\,d}$. Defining $V_{\infty y}$ as the $\hat{d}_2$ component of $\vec{V}_\infty^{\,d}$ and writing the resulting vector in the inertial frame yields:

$$\begin{aligned} \vec{V}_\infty = &\left(-\cos\phi_l \sin w'(r_u,t) - \sin\phi_l \cos w'(r_u,t)\right) V_{\infty y}\hat{n}_1 + \\ &\left(-\sin\phi_l \sin w'(r_u,t) + \cos\phi_l \cos w'(r_u,t)\right) V_{\infty y}\hat{n}_2 \end{aligned} \tag{132}$$

The position vector to any point on the rectangle representing the spar can be written as:

$$\begin{aligned} \vec{r}_{pr} = &\left(-r_r\cos\phi_l - r_u\cos\phi_l - \sin\phi_l\Phi_1\eta_1 - \sin\phi_l\Phi_2\eta_2\right)\hat{n}_1 \\ &+ \left(r_r\sin\phi_l + r_u\sin\phi_l + \cos\phi_l\Phi_1\eta_1 + \cos\phi_l\Phi_2\eta_2\right)\hat{n}_2 + z\hat{n}_3 \end{aligned} \tag{133}$$

From Eqs. 130 and 133 it is shown that both the differential force and the position vector from the origin to the point of application of the differential force are not explicit functions of the generalized coordinate

θ; however, recall that ϕ_l is a function of θ. Thus the chain rule for partial derivation must be used in the determination of the differential contribution to the generalized force associated with the motor angular position. Thus,

$$dQ_{d_\theta} = dF_{Dx}\frac{\partial r_{pr_x}}{\partial \phi_l}\frac{\partial \phi_l}{\partial \theta} + dF_{Dy}\frac{\partial r_{pr_y}}{\partial \phi_l}\frac{\partial \phi_l}{\partial \theta} \tag{134}$$

$$dQ_{d_{\eta_1}} = dF_{Dx}\frac{\partial r_{pr_x}}{\partial \eta_1} + dF_{Dy}\frac{\partial r_{pr_y}}{\partial \eta_1} \tag{135}$$

$$dQ_{d_{\eta_2}} = dF_{Dx}\frac{\partial r_{pr_x}}{\partial \eta_2} + dF_{Dy}\frac{\partial r_{pr_y}}{\partial \eta_2} \tag{136}$$

Thus

$$Q_{d_\theta} = \int_0^L \left(dF_{Dx}\frac{\partial r_{pr_x}}{\partial \phi_l}\frac{\partial \phi_l}{\partial \theta} + dF_{Dy}\frac{\partial r_{pr_y}}{\partial \phi_l}\frac{\partial \phi_l}{\partial \theta} \right) \tag{137}$$

$$Q_{d_{\eta_1}} = \int_0^L \left(dF_{Dx}\frac{\partial r_{pr_x}}{\partial \eta_1} + dF_{Dy}\frac{\partial r_{pr_y}}{\partial \eta_1} \right) \tag{138}$$

$$Q_{d_{\eta_2}} = \int_0^L \left(dF_{Dx}\frac{\partial r_{pr_x}}{\partial \eta_2} + dF_{Dy}\frac{\partial r_{pr_y}}{\partial \eta_2} \right) \tag{139}$$

Note that these generalized forces are state dependent and therefore, these spatial integrals must be evaluated at each simulation time-step by quadrature.

E. Summary of Measured Parameters

Table 1 shows the estimates of the parameters of associated with the drive train elements. The inertias of the gears were estimated by weighing each gear on a precision scale to the nearest 0.1 mg. The gears were constructed in a 3D CAD program and mass moment of inertia properties were estimated using the mass measurement and the computed volume to obtain the density of the material. The inertia of the coreless motor armature was estimated by dissection and measurement. The inside and outside diameter of the copper windings were measured, clipped off and weighed on a scale to the nearest 0.1 mg. Similarly the spindle was measured and weighed separately. The armature assembly was drawn in a 3D CAD program and the mass properties were estimated. It is important to accurately characterize the armature inertia because there is no mechanical advantage at the motor stage to mitigate its effect.

Table 1. Parameters for the motor, gears and encoders

Descriptions	Variables	Values	Units
Stage 1 gear ratio	G_1	9/48	-
Stage 2 gear ratio	G_2	12/81	-
Inertia of stage 1 gear	I_{G_1}	0.032334	g-cm^2
Inertia of stage 2 gear	I_{G_2}	0.25515	g-cm^2
Inertia of encoder	I_e	0.35329	g-cm^2
Inertia of 9-tooth pinion	I_{P9}	0.00013719	g-cm^2
Inertia of 12-tooth pinion	I_{P12}	0.0076397	g-cm^2
Inertia of motor armature	I_a	0.015845	g-cm^2
Motor torque constant	K_T	6774	(dyne-cm)/A
Motor back-EMF constant	K_b	0.000764	V/(rad/sec)
Mechanism friction coefficient	b	0.525	dyne-cm/(rad/sec)
Motor resistance	R_a	2.3	Ω

Table 2 shows the estimates of the parameters of associated with the drive train elements. These estimates were obtained by weighing the linkage elements on a scale to the nearest 0.1 mg and drawing the elements in a 3D CAD package that provides mass property estimates.

Table 2. Parameters for the four-bar linkage

Descriptions	Variables	Values	Units
Line-of-centers length	l_0	-1.936	cm
Crank length (link 1 formed by 81-tooth gear)	l_1	0.461	cm
Link 2 pin-to-pin length	l_2	2.060	cm
Link 3 pin-to-pin length	l_3	0.670	cm
Distance to CG of link 2 from connection point at link 1	l_{c2}	$\frac{1}{2}l_2$	cm
Distance to CG of link 3 from connection point at link 2	l_{c3}	0.753	cm
Distance to root of spar from rocker pivot	r_r	1.735	cm
Mass of pins at linkage joints	m_p	0.025	g
Mass of link 2	m_2	0.1072	g
Mass of link 3	m_3	0.1513	g
Moment of inertia of link 2 about its CG	I_2	0.06165	g-cm^2
Moment of inertia of link 3 about its CG	I_3	0.04283	g-cm^2

Table 3 summarizes the parameter estimates associated with the wing spar.

Table 3. Parameters for the flexible wing spar

Descriptions	Variables	Values	Units
Spar Length	L	13.0	cm
Young's Modulus of Spar	E_s	1.1704×10^{12}	dyn/cm^2
Diameter of spar	d_s	0.0940	cm
Area moment of inertia of spar about neutral axis	I_s	3.8292×10^{-6}	cm^4
Mass per unit length of spar	$\hat{m}$	0.01085	g/cm
Length of spar adjoining rocker arm	l_r	0.556	cm
Modal damping ratio	$\zeta_1 = \zeta_2$	0.025	-

VI. Results

A. Experiment

A bench-test experiment was performed using the mechanism shown in Figure 1 for the purpose of providing a point of comparison for the simulation results. Four time-based measurements were acquired from the experiment, namely, the velocity of the first stage gear via an optical encoder, armature voltage, motor current, and digital images from a high speed camera. Motor voltage, current, and encoder circuit waveforms were recorded by a data acquisition (DAQ) system.

An optical encoder with 16 slots ran at the same speed as the first stage gear, which rotated at 3/16 of the speed of the motor and 27/4 times faster than the speed of the crank gear. This arrangement yielded a resolution of 108 pulses per crank revolution and 3.357 pulses per motor revolution. The time delay between encoder pulses was measured by a 20 MHz clock within the data acquisition system. The pulse periods were measured from falling edge to falling edge. The detection of falling edge pulses also triggered A/D sampling of the instantaneous armature voltage and supply current. A 2000 frame per second camera system captured overhead images of the system against the background of a protractor plate that was centered on the rocker arm pivot. Protractor measurements for the spar tip could be read to the nearest $1/2^\circ$ at low tip velocities; however, the spar appeared blurred over arcs of up to 3° at high tip velocities. Precise measurements of deflection were therefore only taken at the stroke reversal points.

The experiment proceeded by triggering the camera system, applying 2.81 V from a regulated power supply to the motor armature, and recording a 4 second segment of the system response. The polarity of

the voltage applied to the armature resulted in a clockwise crank rotation when viewed by the cameras, which is important to note because the system response is direction dependent. The 4 second segment was sufficient for the system to achieve a long period of steady state operation[f] . When synchronizing the camera clock to the data acquisition system clock, the first frame that motion was detected using the camera system was assumed to correspond to the first frame acquired by the data acquisition system. The accuracy of the time-base synchronization is, therefore, estimated to be within $\pm.0005s$.

B. Comparison of Simulation Results to Experimental Measurements

A segment of the simulation and experimental results for the system under steady-state operation is examined. Figure 6 shows a comparison of simulation time histories and experimental measurements that have been synchronized based upon extremal spar tip displacements. The experimental measurements that are presented here are typical of results that were observed over multiple experimental trials. The middle two displacement traces show the simulated time history of the angular displacement of the rocker arm (blue) and spar tip (green) as would be measured by the background protractor on the bench test platform. The vertical red and blue lines indicate the times at which the extremal spar tip displacements were measured using the high speed camera images. It can be seen that the period of the experimental results matches the period of the simulation results. This match was achieved by fine-tuning the friction coefficient b in the simulation until the crank rotation periods coincided, leaving all other parameters fixed at their measured or computed values. The measured values of the spar tip deflection at the extremal points were extracted from the camera images and appear as red and blue asterisks on the vertical lines associated with stroke reversals. Note that the spar tip deflections associated with the blue asterisks are greater than those associated with the red asterisks. This is because the linkage produces temporally asymmetric motion that results in a stronger reversal on one side than the other. This effect can be seen in the displacement plot as well, where the peaks associated with strong reversals are noticeably sharper than those associated with the weak reversals. The simulated tip deflections compare favorably with those measured by the camera at the extremal points. Finally, the experimentally measured and simulated crank frequencies can be seen in the top two traces. It can be seen that the characteristics of the time histories compare favorably. The simulation slightly under-predicts the peak experimental crank frequency of 14.85 Hz by predicting a value of 13.98 Hz for a difference of 4.9%. The simulation also slightly under-predicts the minimum experimental crank frequency of 11.03 Hz by predicting a value of 11.66 Hz for a difference of 5.7%.

Another measure of the quality of the simulation is to compare "multi-exposure" images taken of the spar as it traverses from one reversal point to another. Figure 7 shows a comparison of enhanced camera images and the simulation images for the spar as it traverses from the weak to the strong reversal point for clockwise crank rotation. Reflections and blurred images obscure the spar in some segments of the motion, thus, the images have been enhanced by the use of a sketch overlay in order to improve the visibility of the spar. The sketched overlay was produced by carefully tracing over the centerline of each spar image with a solid black digital "pen" using image processing software. The images shown in Figure 7 correspond to the portion of the time histories between 0.802 sec and 0.841 sec shown in Figure 6. The most striking feature of the images is the "dwell" that occurs near the 60° mark. Another less significant dwell can be seen between 95° and 105°. This dwell effect is not readily discernable from time history plots of state variables; however, the effect is a prominent feature of the motion that can be seen when viewing video images from the high speed camera system. The appearance of the dwell phenomenon is a result of the combined motion of the flexible structure and the rocker arm. In the dwell regions, the spar is moving backwards relative to the rocker arm as a result of dynamic structural deformation. Clearly, the presence of such dwell regions have a significant effect upon the local dynamic pressure experienced by the spar and the resulting aerodynamic loads.

[f]Defined as a condition where the period of crank rotation is constant from one wing beat cycle to the next

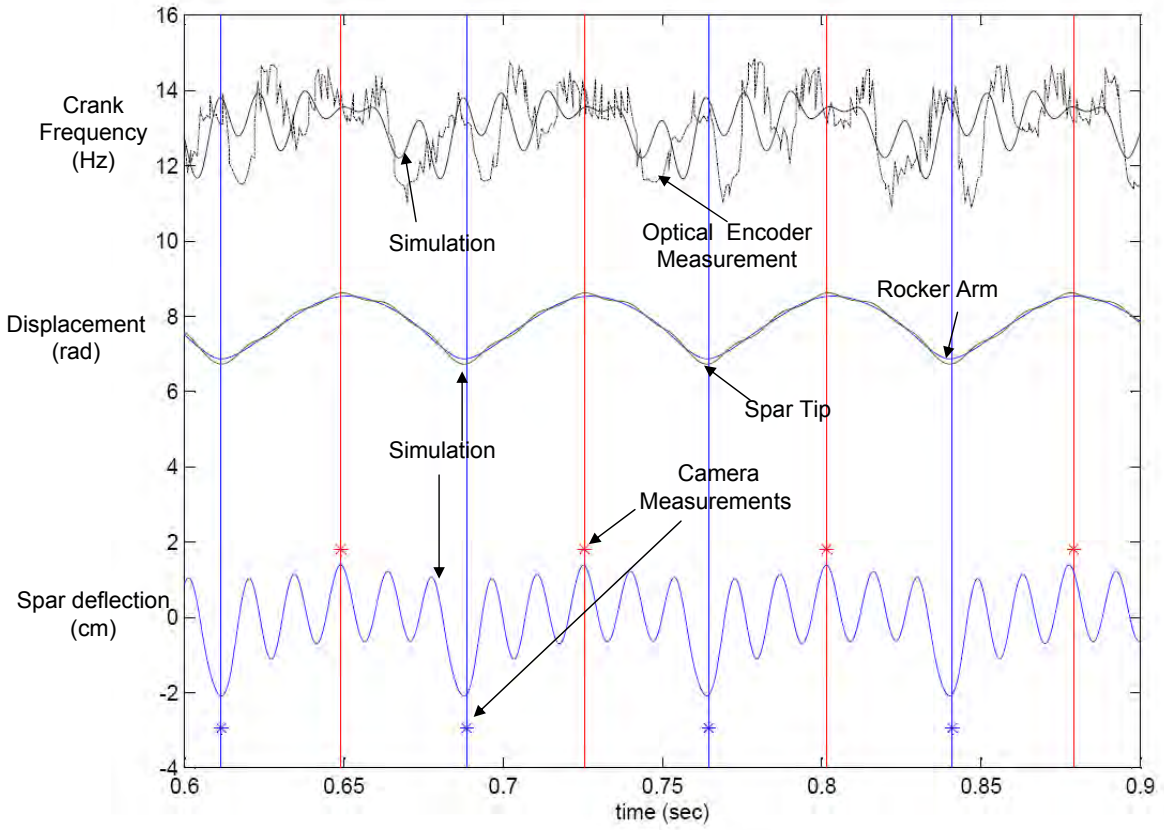

Figure 6. Comparison of Experimental and Simulation Results

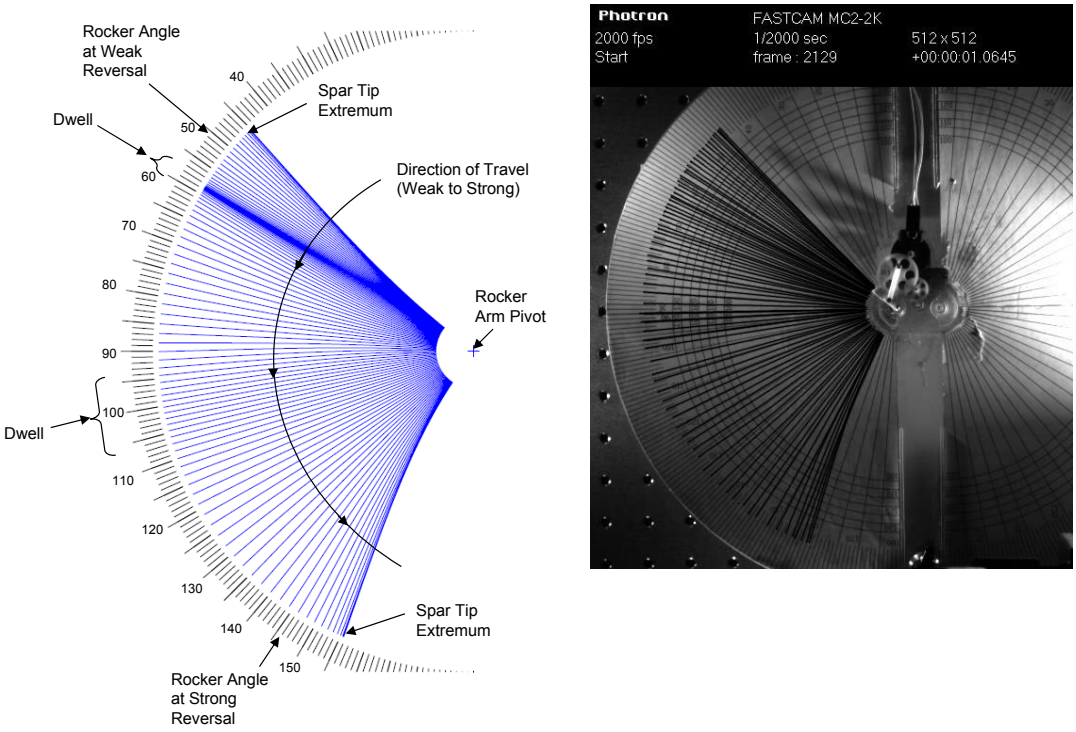

(a) Simulation (b) 2000 FPS Camera (Sketch overlay)

Figure 7. Multi-exposure comparison on downstroke (weak to strong)

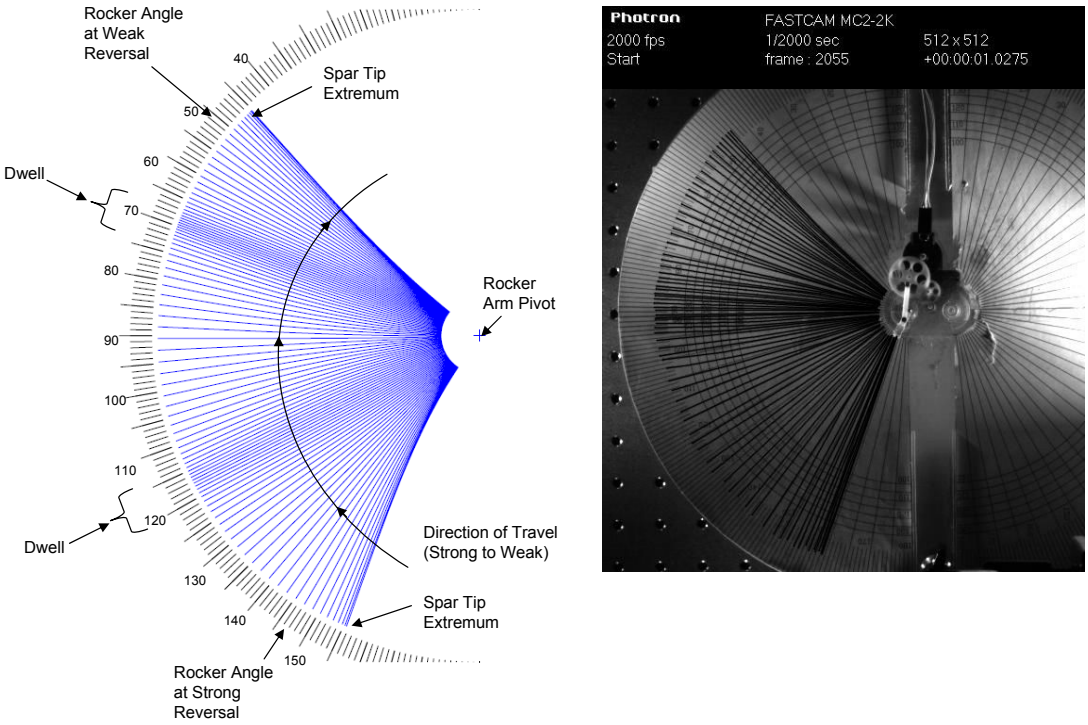

(a) Simulation

(b) 2000 FPS Camera (Sketch overlay)

Figure 8. Multi-exposure comparison on upstroke (strong to weak)

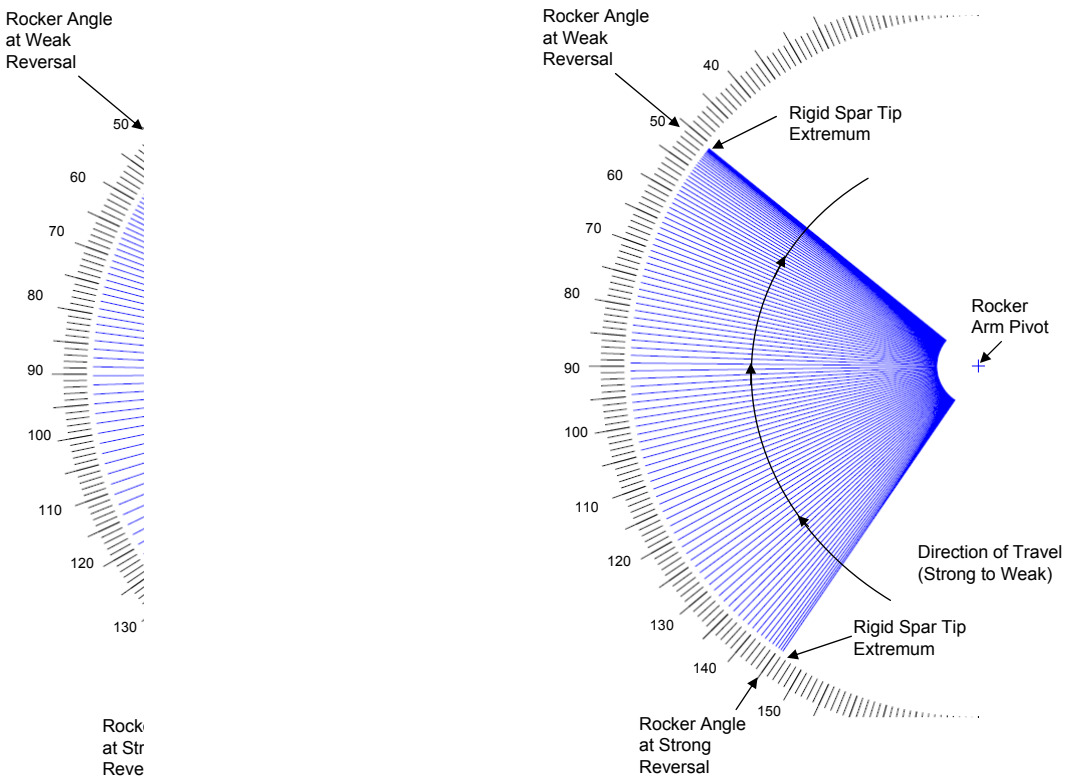

(b) Strong to Weak

Figure 9. Naive simulation, constant velocity motor, rigid spar

The impact of the modeling error associated with the kinematic simulation on aerodynamic loads can be assessed by comparing the behavior of two time varying integrals over the course of a wingbeat. The magnitude of an arbitrary aerodynamic load, F, created by a dynamic pressure distribution over the length of the spar is given by:

$$F = \frac{1}{2}\rho C_F d_s \int_0^L V^2(r_u, t) dr_u \tag{140}$$

If over the course of a wingbeat, the terms premultiplying the velocity squared integral are taken to be constant, then the differences between the integrals for the kinematic simulation and the dynamic simulation are a measure of the differences in instantaneous aerodynamic force. For the full dynamic simulation,

$$\int_0^L V^2(r_u, t) dr_u = c_1 S_2^2 \dot{\theta}^2 + c_2(S_2^2 \dot{\theta}^2 \eta_1^2 + \dot{\eta}_1^2) + 2c_4 S_2 \dot{\theta} \dot{\eta}_1 + c_7(S_2^2 \dot{\theta}^2 \eta_2^2 + \dot{\eta}_2^2) + 2c_8 S_2 \dot{\theta} \dot{\eta}_2 \tag{141}$$

whereas for the kinematic simulation,

$$\int_0^L V_k^2(r_u, t) dr_u = c_1 S_2^2 \dot{\theta}^2 \tag{142}$$

A plot that compares the two integrals over the course of a wingbeat is shown in Figure 10. It can be seen that the flexible dynamics significantly influence the value of this integral and therefore the magnitude of the aerodynamic loads. It was found that the cycle-averaged value of the integral from the dynamic simulation was $3.1659 \times 10^6 \text{cm}^2/\text{sec}^2$, while the value corresponding to the kinematic simulation results was $2.5511 \times 10^6 \text{cm}^2/\text{sec}^2$, which indicates that the aerodynamic loads produced by the flexible spar would be about 24% higher than those predicted by a simple kinematic simulation. It can be concluded that despite fluctuations in the motor speed and the presence of dwell regions, the flexible spar produces higher average aerodynamic loads than the rigid spar. The higher loads are the result of an increase in effective stroke amplitude and velocity near the stroke reversal points.

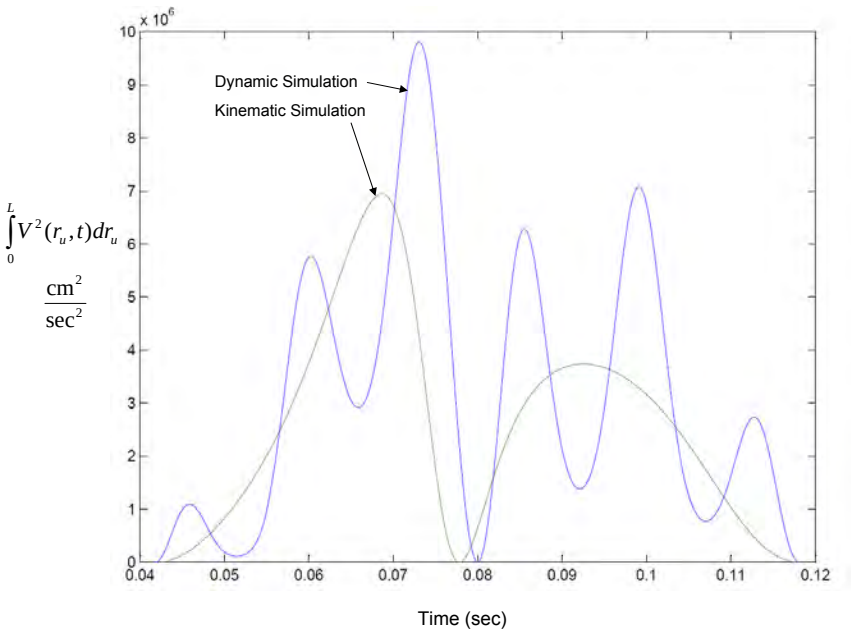

Figure 10. Behavior of velocity squared integral, related to magnitude of aerodynamic forces

An additional observation was that the inclusion of the dynamics of the second bending mode, in this particular case, was not warranted. A short study was conducted where all terms in Eq. 118 that were associated with the second bending mode were set to zero. The simulation results generated by the model that included the rigid body coordinate and the first bending mode were visually indistinguishable from those shown in Figures 6, 7, 8, and 10. Furthermore the change in the cycle averaged value of the velocity squared integral occurred in the 4^{th} decimal place, i.e. $3.1656 \times 10^6 \text{cm}^2/\text{sec}^2$ for the single mode versus $3.1659 \times 10^6 \text{cm}^2/\text{sec}^2$ for the second mode.

This work considers the dynamic coupling between ornithopter subsystems from the motor to the wing spar. In order to analyze a system that includes wing ribs and membrane elements, at least two additional degrees-of-freedom should be considered, viz., wing torsion, and out-of-plane bending. An analysis that includes these additional wing elements is beyond the scope of the present paper and will be considered in future work.

VII. Conclusions

From the comparison of the simulation and experimental results, it is concluded that the Lagrangian analysis method captures the major features and trends observed in the experiment significantly better than constant velocity motor and rigid spar kinematic simulations used by previous investigators. Furthermore, it is concluded that dynamic interactions between the flexible wing elements, drive-train, and motor, have a significant effect upon both the instantaneous and cycle-averaged aerodynamic loads upon the spar. Thus, when designing machines to optimize wing motion or attempting to match wing stroke patterns observed in natural flyers, one must consider coupling between drive components and the wings rather than simply prescribing wing kinematics. The validation of the equations of motion by comparing simulation results to experimental measurements, instills confidence in the accuracy of the model. It was also found, that in the specific case considered in the experiment, the second bending mode had little effect upon the model predictions. It is therefore expected that in many cases, it may be possible to ignore second bending mode effects and still maintain an adequate level of accuracy. Although the model was validated on a single test bed, the modeling framework is applicable to a large class of MAV ornithopters. The equations of motion presented in this paper can be used to predict how DC motor powered flapping wing micro air vehicle (MAV) subsystem elements will behave when a constant or time varying voltage is applied to the motor armature. These equations provide a powerful analysis tool for MAV system designers because they can be used as the basis for a systematic method of selecting motors, drive-trains, linkage kinematics, and designing structural and aerodynamic properties of flapping wing MAVs. They also have the potential to support mechanism control law designs that can improve the behavior of wingbeat motion over what could be achieved by simply applying a constant voltage to the drive motor.

VIII. Acknowledgements

The authors would like to recognize the efforts of Benjamin Perseghetti, Kyle Carson, and 1 Lt. Eric Wolf for their support in the construction of the test article and for taking measurements of vehicle components. Michael Porter from Data Science Automation is acknowledged for the design and construction of the optical encoder, the non-contact proximity sensor, and for programming the LabVIEW Virtual Instruments that made it possible to record the experimental data. The experimental research was conducted in the AFRL microAVIARI facility at Wright Patterson AFB, OH. The overall research project was supported under a lab task administered by the Air Force Office of Scientific Research, Dr. Fariba Fahroo, program manager.

IX. Appendix

A. Differentiation of the Configuration Dependent Terms in the Four-Bar Linkage

In order to evaluate Eq. (101) the following relationships are required:

$$\frac{\partial S_1}{\partial \theta} = -\Gamma^2 \frac{l_1}{l_2} \frac{\cos(\phi_l - \Gamma\theta)}{\sin(\alpha_l - \phi_l)} \tag{143}$$

$$\frac{\partial S_1}{\partial \alpha_l} = -\Gamma \frac{l_1 \cos(\alpha_l - \phi_l)\sin(\phi_l - \Gamma\theta)}{l_2 \sin^2(\alpha_l - \phi_l)} \tag{144}$$

$$\frac{\partial S_1}{\partial \phi_l} = \Gamma \frac{l_1 \sin(\alpha_l - \Gamma\theta)}{l_2 \sin^2(\alpha_l - \phi_l)} \tag{145}$$

$$\frac{\partial S_2}{\partial \theta} = -\Gamma^2 \frac{l_1}{l_3} \frac{\cos(\alpha_l - \Gamma\theta)}{\sin(\alpha_l - \phi_l)} \tag{146}$$

$$\frac{\partial S_2}{\partial \alpha_l} = -\Gamma \frac{l_1 \sin(\phi_l - \Gamma\theta)}{l_3 \sin^2(\alpha_l - \phi_l)} \tag{147}$$

$$\frac{\partial S_2}{\partial \phi_l} = \Gamma \frac{l_1 \sin(\alpha_l - \Gamma\theta)\cos(\alpha_l - \phi_l)}{l_3 \sin^2(\alpha_l - \phi_l)} \tag{148}$$

$$\frac{\partial C_1}{\partial \theta} = -\Gamma \sin(\Gamma\theta - \alpha_l) \tag{149}$$

$$\frac{\partial C_1}{\partial \alpha_l} = \sin(\Gamma\theta - \alpha_l) \tag{150}$$

References

[1]Weis-Fogh, T. and Jensen, M., "Biology and Physics of Locust Flight, 1: Basic Principles in Insect Flight. A Critical Review," *Proceedings of the Royal Society of London, Series B: Biological Series*, Vol. 239, No. 667, 1956. pp. 415–458

[2]Ellington, C. P., "The Aerodynamics of Hovering Insect Flight, Parts I-VI," *Philosophical Transactions of the Royal Society of London: Series B: Biological Series*, Vol. B305, No. 4, 1984. pp 1–181.

[3]Thomas A.L.R. and Taylor G.K., "Animal Flight Dynamics I. Stability in Gliding Flight," *Journal of Theoretical Biology*, Vol. 212, No. 3, 2001. pp. 399–424

[4]Taylor G.K. and Thomas A.L.R., "Animal Flight Dynamics II. Longitudinal Stability in Flapping Flight," *Journal of Theoretical Biology*, Vol. 214, No. 3, 2002. pp. 351–370

[5]Shyy, W., Lian, Y, Tanj, J., Viieru, D., and Liu, H., *Aerodynamics of Low Reynolds Number Flyers*, Cambridge University Press, New York, NY, 2008. pp. 1–27

[6]de Croon, G.C.H.H., de Clercq, K.M.E., Ruijsink, R., Remes, B., and de Wagter, C., "Design, Aerodynamics, and Vision-Based Control of the DelFly," *International Journal of Micro Air Vehicles*, Vol. 1, No. 2, Jun. 2009. pp. 71–97

[7]Jones, K.D., Bradshaw, C.J., Papadopoulos, J., and Platzer, M.F., "Bio-inspired Design of Flapping-Wing Micro Air Vehicles," *The Aeronautical Journal*, Vol. 109, No. 1098, Aug. 2005. pp. 385–393

[8]Gerdes, J. W., Gupta, S. K., and Wilkerson, S. A., "A Review of Bird-Inspired Flapping Wing Miniature Air Vehicle Designs," *Proceedings of the ASME Design Engineering and Technical Conferences*, Paper No. DETC2010-28513, Montreal, Quebec, Canada, Aug. 2010. pp. 57–67

[9]Doman, D. B. and Regisford, S., "Wing Sizing, Trim, and Control Consideration in the Design of Hover-Capable Flapping Wing Micro Air Vehicles," AIAA Paper 2010-7629, Aug. 2010.

[10]Madangopal, R., Khan, Z. A., and Agrawal, S. K., "Energetics-Based Design of Small Flapping-Wing Micro Air Vehicles," *IEEE/ASME Transactions on Mechatronics*, Vol. 11, No. 4, Aug. 2006, pp. 433–438.

[11]McDonald, M. and Agrawal, S. K., "Design of a Bio-Inspired Spherical Four-Bar Mechanism for Flapping-Wing Micro-Air-Vehicle Applications," *ASME Journal of Mechanisms and Robotics*, Vol. 2, No. 2, May 2010. pp. 945–953

[12]Rehmat, Z., Roll, J., Lee, J. S., Yim, W., and Trabia, M. B., "Design of "Figure-8" Spherical Motion Flapping Wing for Miniature UAV," *Proceedings of the ASME Design Engineering and Technical Conferences*, San Diego, California, USA, Aug.-Sep. 2009. pp. 539–546

[13]Trabia, M. B., Yim, W., Rehmat, Z., and Roll, J., "Flight Characteristics of Flapping Wing Miniature Air Vehicles with "Figure-8" Spherical Motion," *Proceedings of the ASME International Mechanical Engineering Congress and Exposition*, Buena Vista, Florida, USA, November 2009. pp. 293–300

[14]Raney, D.L. and Slominski, E.C., "Mechanization and Control Concepts for Biologically Inspired Micro Air Vehicles," *Journal of Aircraft*, Vol. 41, No. 6, 2004. pp. 1257–1265

[15]Chung, S.J., Stoner, J.R., and Dorothy M., "Neurobiologically Inspired Control of Engineered Flapping Flight," AIAA Paper 2009-1929, Apr. 2009.

[16]Berman, G. and Wang, Z., "Energy-Minimizing Kinematics in Hovering Insect Flight," *Journal of Fluid Mechanics*, Vol. 582, pp. 153–168.

[17]Kurdi, M., Stanford, B., and Beran, P., "Kinematic Optimization of Insect Flight for Minimum Mechanical Power," AIAA Paper 2010-1420, Jan. 2010.

[18]Soueid, H., Guglielmini, L., Airiau, C., and Bottaro, A., "Optimization of the Motion of a Flapping Airfoil Using Sensitivity Functions," *Computers and Fluids*, Vol. 38, No. 4, 2009, pp. 861–874.

[19]Deng, X., Schenato, L., Wu, W.C., and Sastry, S.S., "Flapping Flight for Biomimetic Robotic Insects: Part I – System Modeling," *IEEE Transactions on Robotics*, Vol. 22, No. 4, Aug. 2006. pp. 776–788

[20]Deng, X., Schenato, L., and Sastry, S.S., "Flapping Flight for Biomimetic Robotic Insects: Part II – Flight Control Design," *IEEE Transactions on Robotics*, Vol. 22, No. 4, Aug. 2006. pp. 789–803

[21]Khan, Z.A. and Agrawal, S.K., "Control of Longitudinal Flight Dynamics of a Flapping-Wing Micro Air Vehicle Using Time-Averaged Model and Differential Flatness Based Controller," *Proceedings of the American Control Conference*, IEEE, Jul. 2007. pp. 5284–5289

[22]Dileo, C. and Deng, X., "Design of and Experiments on a Dragonfly-Inspired Robot," *Advanced Robotics*, Vol. 23, No. 7-8, 2009. pp. pp. 1003–1021

[23]Wood, R.J., Avadhanula S., M. and Fearing R.S., "Microrobotics using Composite Materials: The Micromechanical Flying Insect Thorax," *Proc. IEEE Intl. Conf. on Robotics and Automation*, Vol. 2, IEEE Press, Piscataway, NJ, 2003, pp. 1842–1849.

[24]Wood, R., "The First Takeoff of a Biologically Inspired At-Scale Robotic Insect," *IEEE Transactions on Robotics*, Vol. 24, No. 2, 2007, pp. 341–347.

[25]Avadhanula, S., Wood, R., Campolo, D., and Fearing, R., "Dynamically Tuned Design of the MFI Thorax," *IEEE Int. Conf. on Robotics and Automation*, Vol. 1, May 2002. pp. 52–59

[26]Ogata, K., *Modern Control Engineering, 2nd Ed*, Prentice Hall, Englewood Cliffs, NJ, 1990. pp. 118–122

[27]Meirovitch, L., *Analytical Methods in Vibrations*, The Macmillan Company, New York, NY, 1967. pp. 161–166, 233–235

[28]Craig, R. R., *Fundamentals of Structural Dynamics*, John Wiley, Hoboken, NJ., 2006. p. 35

[29]Greenwood, D. T., *Principles of Dynamics, 2nd Ed.*, Prentice Hall, Upper Saddle River, NJ, 1988. pp. 259–262

[30]Osborne, M., "Aerodynamics of Flapping Flight with Application to Insects," *Journal Experimental Biology*, Vol. 28, pp. 221–245.